Surface and borehole ground-penetrating-radar developments

Evert Slob[1], Motoyuki Sato[2], and Gary Olhoeft[3]

ABSTRACT

During the past 80 years, ground-penetrating radar (GPR) has evolved from a skeptically received glacier sounder to a full multicomponent 3D volume-imaging and characterization device. The tool can be calibrated to allow for quantitative estimates of physical properties such as water content. Because of its high resolution, GPR is a valuable tool for quantifying subsurface heterogeneity, and its ability to see nonmetallic and metallic objects makes it a useful mapping tool to detect, localize, and characterize buried objects. No tool solves all problems; so to determine whether GPR is appropriate for a given problem, studying the reasons for failure can provide an understanding of the basics, which in turn can help determine whether GPR is appropriate for a given problem. We discuss the specific aspects of borehole radar and describe recent developments to become more sensitive to orientation and to exploit the supplementary information in different components in polarimetric uses of radar data. Multicomponent GPR data contain more diverse geometric information than single-channel data, and this is exploited in developed dedicated imaging algorithms. The evolution of these imaging schemes is discussed for ground-coupled and air-coupled antennas. For air-coupled antennas, the measured radiated wavefield can be used as the basis for the wavefield extrapolator in linear-inversion schemes with an imaging condition, which eliminates the source-time function and corrects for the measured radiation pattern. A handheld GPR system coupled with a metal detector is ready for routine use in mine fields. Recent advances in modeling, tomography, and full-waveform inversion, as well as Green's function extraction through correlation and deconvolution, show much promise in this field.

INTRODUCTION

Ground-penetrating radar (GPR) — also known as georadar, subsurface radar, and ground-probing radar — is a geophysical method of obtaining information about the subsurface with extremely high resolution. Several comprehensive textbooks discuss the technique (Conyers and Goodman, 1997; Bristow and Jol, 2003; Daniels, 2004; Jol, 2009).

GPR waves are sensitive to changes in the subsurface and to GPR data contrasts in electrical and magnetic properties; such changes can be detected, imaged, and characterized. GPR's high frequency makes it insensitive to electrochemical reactions seen at lower frequencies, but the resulting high resolution makes it sensitive to physics and geometry, texture, and structure, which are very useful in understanding and describing heterogeneity (Olhoeft, 1991a, 1991b). Its depth of penetration ranges from 5400 m in polar ice to less than 1 m in wet bentonite clay, with typical ranges of 10–30 m in sand. It works well below the water table in clay-free freshwater environments and through nonmineralogical clay (rock flour) to depths of 30 m.

GPR is one of the few techniques sensitive to changes in water and nonmetallic materials, and it has a still-increasing number of applications. Instead of writing an historic overview, which has been done by Annan (2002, 2005), we provide an overview of the applications that have been developed over the years. Surface and borehole GPR have found applications in glacier (Stern, 1929) and polar ice (Bailey et al., 1964; Robin et al., 1969) mapping; aquifer characterization and hydrogeology (Barringer, 1965; Beres and Haeni, 1991); planetary exploration on Mars and the moon (Simmons et al., 1972); salt exploration (Thierbach, 1974; Mundry et al., 1978); coal mining (Cook, 1977); geotechnical, hydrological, and environmental problems (Benson, 1979; Owen and Suhler, 1982; Sandness and Kimball, 1982); detecting thawing zones in permafrost areas (Olhoeft, 1980); mine-efficiency improvements (Nickel et al., 1983; Niva et al., 1988); pavement and railroad ballast problems (Rodeick, 1984; Maser, 1986; Olhoeft et al., 2004); archaeology (Vaughan, 1986; Be-

van, 1991); fracture mapping (Olsson et al., 1985; Holloway et al., 1986; Grasmueck, 1996); agriculture (Collins and Doolittle, 1987; Allred et al., 2008); geomorphology (Leatherman, 1987); tunnel detection (Greenfield, 1988; Olhoeft, 1988); stratigraphy and sedimentology (Hsi-Tien, 1989; Davis and Annan, 1989; Schenk et al., 1993); subsurface utility mapping (Liu and Shen, 1991); land-mine and unexploded ordnance (UXO) detection (Olhoeft et al., 1994); and forensics investigations (Owsley, 1995). The references listed here cite some early work or refer to reference books and by no means are a full account of all activities.

The fact that GPR works so well in the above-mentioned applications is because of the wave-propagation nature of GPR in combination with its sensitivity to changes in electromagnetic (EM) material properties — particularly to changes in the presence of water. Many applications of GPR are detection applications, where minimal signal processing is required and interpretation can be carried out on the recorded data from which the low-frequency content is filtered out (dewow). For applications where some quantification is desired (burial depth, size and orientation of object, moisture content, etc.), imaging and/or inversion is necessary. One of the earliest theoretical developments is presented in Annan (1973). Modeling, imaging and tomography, and inversion of GPR data are active fields of research. Because GPR relies on wave propagation, many methods that have been developed for seismic exploration have been adapted (because GPR and seismic have important differences) and used for GPR (Liu and Shen, 1991; Fisher et al., 1992a; Goodman, 1994; Witten et al., 1994). Specific applications require that data be recorded close to a deep target, and this is achieved using GPR in or between boreholes.

Our paper starts with a section on the principles of GPR where the material properties to which electromagnetic waves are sensitive are discussed, followed by a brief discussion on propagation and scattering effects and a simple rule for estimating system performance. Special attention is given to borehole GPR because of the physical limitation of a borehole. The consequences of antenna design and associated challenges are described. This is followed by discussions on polarimetric use of borehole GPR and dedicated imaging and inversion methods for crosshole data. The developments that have led to migration and linear-inversion algorithms dedicated to EM waves are discussed, and imaging GPR data from ground- and air-coupled acquisition configurations is described. We treat one case study, choosing the humanitarian demining application of GPR because it is recent and has been developed to the level where it can be used routinely. The section on present and future developments briefly describes the current regulatory environment under which GPR must be used as well as new developments in modeling, inversion, tomography, and data-driven methods for extracting Green's function and redatuming GPR sources.

PRINCIPLES OF GPR

Every measurement assumes an underlying theoretical model. Without a theoretical model, a measurement result cannot be given meaning. Using GPR for subsurface applications therefore requires understanding how the EM waves that we use to obtain subsurface properties respond to changes in the subsurface. Because the used field strengths cause small enough disturbances relative to the existing equilibrium field, the subsurface responds linearly to the radar wave. We also assume the subsurface does not change in time over the duration of a single measurement. Because of these two conditions, subsurface GPR applications are investigations on a linear,

time-invariant (LTI) system. Hence, all measurements can be understood from linear-system theory, and all operations that we apply are filters that can be understood from filter theory. This does not preclude time-lapse measurements (Greenhouse et al., 1993) but only requires the system to change slowly (hours) compared to the time of measurement (milliseconds).

As a direct consequence of the LTI system condition, the measured field strengths are linearly proportional to the applied source strengths, and medium property functions are independent of the amplitude of the applied fields and sources. They may depend on time relative to a reference-time instant, usually chosen as the time when the transmitter is switched on. This allows for modeling all kinds of time-relaxation phenomena, which can be formulated mathematically by writing the medium property that shows time relaxation as a time-convolution operator — a notion going back to Boltzmann (1876). A second direct consequence of the LTI system condition is that all time interactions are described by convolutions, and time can be transformed conveniently to frequency. The advantage of such a transformation is that time convolutions of two time-dependent functions transform to products of these frequency-dependent functions in the frequency domain, and the time-derivative operator is reduced to an algebraic factor.

Electrical and magnetic material properties

If a medium's property function is a constant, the medium is said to be homogeneous; if it varies as a function of position in space, it is said to be heterogeneous or inhomogeneous. A homogeneous medium is shift invariant, meaning that only the distance between two points is relevant but absolute positions are not. For such media, a spatial Fourier transformation can be carried out with similar benefits as for the time-Fourier transformation. If a medium's property function does not depend on orientation, the medium is said to be isotropic, whereas an anisotropic medium has a property function that is orientation dependent.

For an anisotropic medium, the EM medium's property functions are tensors of rank two. Generally, we use a macroscopic model wherein the electric current density, the electric displacement current, and the magnetic flux density are proportional to the electric and magnetic fields. We use subscript notation. A vector is written with a lowercase Latin subscript to indicate the three vector components; the summation convention applies to repeated subscripts. We can write

$$J_k(\mathbf{x},t) = \int_{\tau=0}^{t} \sigma_{kr}(\mathbf{x},\tau)E_r(\mathbf{x},t-\tau)\mathrm{d}\tau, \Leftrightarrow$$

$$\hat{J}_k(\mathbf{x},\omega) = \hat{\sigma}_{kr}(\mathbf{x},\omega)\hat{E}_r(\mathbf{x},\omega)$$

$$D_k(\mathbf{x},t) = \int_{\tau=0}^{t} \varepsilon_{kr}(\mathbf{x},\tau)E_r(\mathbf{x},t-\tau)\mathrm{d}\tau, \Leftrightarrow$$

$$\hat{D}_k(\mathbf{x},\omega) = \hat{\varepsilon}_{kr}(\mathbf{x},\omega)\hat{E}_r(\mathbf{x},\omega),$$

$$B_p(\mathbf{x},t) = \int_{\tau=0}^{t} \mu_{pq}(\mathbf{x},\tau)H_q(\mathbf{x},t-\tau)\mathrm{d}\tau, \Leftrightarrow$$

$$\hat{B}_p(\mathbf{x},\omega) = \hat{\mu}_{pq}(\mathbf{x},\omega)\hat{H}_q(\mathbf{x},\omega) \qquad (1)$$

where $\mathbf{x}$, t denotes the position vector in 3D space and time, respectively; $\omega = 2\pi f$ denotes radial frequency, with f being natural frequency; J_k, D_k, and B_p denote the time-domain vector components of the electric-current density, the electric-displacement current, and the magnetic-flux density, respectively; E_r and H_q denote the vector components of the electric and magnetic field strengths; and σ_{kr}, ε_{kr}, and μ_{pq} denote the tensor components of the electric conductivity, the electric permittivity, and the magnetic permeability of the medium, respectively. The quantities with the diacritical hats (carets) are the frequency-domain equivalents of the time-domain quantities. The time-integration bounds in equation 1 show the causality conditions satisfied by the fields and the medium's property functions, for which reason the quantities on the left-hand sides of the left column in equation 1 are causal time functions as well.

The free-space parameters are defined as isotropic parameters and have the subscript zero to denote free-space values:

$$\sigma_0 = 0 \text{ Sm}^{-1}, \quad \mu_0 = 4\pi \times 10^{-7} \text{ Hm}^{-1}, \qquad (2)$$

$$\varepsilon_0 = \frac{1}{\mu_0 c_0^2} \text{ Fm}^{-1}.$$

The new parameter in the definition of the electric permittivity is the free-space propagation velocity, which is given by $c_0 = 299{,}792{,}458$ m/s (by definition). Most rocks and soils are multicomponent fluid-filled porous media, and their electric and magnetic properties depend on the properties of the components and their specific mixtures and on the texture — and probably many other details. How these dependencies can be understood is a topic of research in itself; for EM parameters, we refer to texts by von Hippel (1954), Choy (1999), Sihvola (1999), and Milton (2002). To understand the EM parameters in terms of desired physical parameters is beyond the scope of our paper, although it is important to note that whenever the properties deviate from those of free space, they must become complex quantities and frequency dependent and may become nonlinear and hysteretic.

Assuming a homogeneous isotropic medium and wave-propagation factor $\exp(-ikR)$, where R is radial distance, the wavenumber of propagation is a complex function of frequency given by (Balanis, 1988)

$$ik = i\omega\sqrt{\hat{\varepsilon}^*\hat{\mu}^*} = \alpha + \frac{i\omega}{c}, \qquad (3)$$

where $\hat{\varepsilon}^*$ and $\hat{\mu}^*$ are the generalized complex electric permittivity and magnetic permeability, respectively, and α is the positive real coefficient of attenuation that represents the part of the EM wave energy that is irreversibly converted into heat.

Mathematically, the conductivity can be incorporated in the permittivity and expressed as a complex number $\hat{\varepsilon}^* = \hat{\varepsilon} - i\hat{\sigma}/\omega = \varepsilon_0(\varepsilon' - i\varepsilon'')$. We also express the magnetic permeability as a general complex function $\hat{\mu}^* = \mu_0(\mu' - i\mu'')$. The general expressions for the attenuation coefficient and propagation velocity are then given by

$$\alpha = \frac{\omega}{c_0}\left(\frac{|\varepsilon'\mu' - \varepsilon''\mu''|}{2}\right)^{1/2}\left[\left(1 + \left(\frac{\varepsilon'\mu'' + \varepsilon''\mu'}{\varepsilon'\mu' - \varepsilon''\mu''}\right)^2\right)^{1/2}\right.$$
$$\left. - \text{sign}(\varepsilon'\mu' - \varepsilon''\mu'')\right]^{1/2}$$

$$c = c_0\left(\frac{2}{|\varepsilon'\mu' - \varepsilon''\mu''|}\right)^{1/2}\left[\left(1 + \left(\frac{\varepsilon'\mu'' + \varepsilon''\mu'}{\varepsilon'\mu' - \varepsilon''\mu''}\right)^2\right)^{1/2}\right.$$
$$\left. + \text{sign}(\varepsilon'\mu' - \varepsilon''\mu'')\right]^{-1/2}, \qquad (4)$$

and all square roots must be taken positive.

Frequency dependence is the result of the irreversible process of converting EM wave energy into heat through conduction or relaxation processes or from scattering. Dielectric relaxation losses are primarily caused by the presence of water (von Hippel, 1954) and can be enhanced by the presence of clay minerals (Olhoeft, 1987). The magnetic properties of iron oxides can cause GPR reflections (van Dam and Schlager, 2000; van Dam et al., 2002). The ratio of the imaginary and real parts of the material property is known as the loss tangent because it represents an angle in the complex plane. Magnetic and electric loss tangents can be computed as $\tan\delta^m = \mu''/\mu'$, $\tan\delta^e = \varepsilon''/\varepsilon'$. Magnetic relaxation losses are caused by the presence of iron minerals, and both usually follow a Cole-Cole frequency dependence (Olhoeft and Capron, 1994) with a slope of log loss tangent versus log frequency between zero and ± 1. Electrical conduction losses always have a slope of -1. Scattering losses always have a slope much greater than one. Frequency dependence causes the earth to act as a low-pass filter, altering pulse shape as well as amplitude with propagation distance (sometimes called pulse broadening).

For most earth materials, the magnetic permeability can be taken as the free-space value. Further simplification is obtained when we assume the electric permittivity and conductivity have constant values and $\hat{\varepsilon}^* = \varepsilon_0(\varepsilon' - i\sigma/(\omega\varepsilon_0))$ and when we assume $\sigma \ll \omega\varepsilon_0$. Then equation 4 reduces to

$$\alpha = \frac{Z_0\sigma}{2\sqrt{\varepsilon'}}, \quad c = \frac{c_0}{\sqrt{\varepsilon'}}, \qquad (5)$$

where $Z_0 = \sqrt{\mu_0/\varepsilon_0}$ denotes the free-space plane-wave impedance. The result in equation 5 is used by many people and is a good approximation in applications where GPR works well.

Another derived parameter of interest is wavelength, defined as $\lambda = 2\pi/\Re(k) = c/f$, where $\Re(k)$ means the real part of k. Wavelength is an important parameter for determining scattering properties and resolution. At long wavelengths (low frequencies) compared to the size of the scattering target, quasi-static Rayleigh scattering occurs; at wavelengths comparable to the target size, resonance occurs; and at short wavelengths, optical scattering occurs.

Propagation and scattering

Any antenna is made to optimize the transition of the EM wave, put into a cable by the signal generator, from the cable into the world with the least possible disturbance of the signal. A ground-coupled GPR antenna is optimized to emit this wave into the ground. Once the EM wave leaves the transmitter antenna, some part of the field leaks through the air directly to the receiver antenna (direct airwave) and is scattered from nearby above-ground objects (despite possible

attempts to shield the antenna). The wavefield above and below ground may travel between the antennas by multiple paths. The above-ground wavefield will travel with the speed of light in air, which is known, is always faster than in the ground, and thus is easily recognized in multioffset data or in fixed-offset data when it occurs as a hyperbolic event. The wavefield below ground travels through the earth materials with the speed of light in the material, and part of that wave directly travels to the receiving antenna (direct ground wave).

On its propagation path, the wavefield amplitude decreases by geometric spreading and material-attenuation losses. At some point, the wavefield is scattered in the form of reflection, refraction, or diffraction because the wave encounters a change in electric or magnetic properties. A fraction of the wavefield is returned to the receiver; path-loss considerations similar to those from the transmitter apply here as well. The total effect of changes in amplitude from material losses is the result of energy loss by surface scattering at interfaces, by volume scattering from inhomogeneous materials, and by exponential thermal-conversion losses from electrical conduction and from dielectric and magnetic relaxation processes in the material volume through which the wavefield passes along the paths from the transmitter to the scattering object and back to the receiver. These losses vary along different paths, and the frequency, angular orientation, and polarization dependencies can be used to identify the type of loss.

The fraction of the EM wavefield that is returned to the radar system from the subsurface scattering object is determined by the contrast in electric and magnetic properties at an interface between an object and its embedding media. For objects large relative to the wavelength, this is commonly given by the single-interface Fresnel reflection coefficient (Balanis, 1988), which has special cases for layers that are thin compared to the apparent wavelength (Tsang et al., 1985) and that have cross-sectional areas that are small compared to the wavelength. Snell's law describes the amount of energy transmitted through or reflected from a contrasting interface as a function of incidence angle; it varies with polarization. For dissipative media, the angles are complex (Balanis, 1988).

The polarization of an EM wave and the type of polarization incident on a contrasting interface, the high aspect ratio of an object (wire or fracture), or a periodic pattern in a sedimentary sequence also determines the amount and direction of wave scattering. These dependencies are described by the Stokes matrix (van Zyl and Ulaby, 1990). Several commercial radar systems separate transmitter from receiver antennas or provide antennas at different orientations inside one antenna box. With such systems, full-polarization data can be recorded. Many other commercial radar systems do not offer all possible transmitter-receiver polarization combinations and usually only offer linear copolarized electric-field antennas. However, even with such systems, it is possible to rotate the antennas and exploit their polarization properties, e.g., to see rebar in concrete (to assess rebar condition) or to see past the rebar to ascertain concrete thickness. In the first case, the rebar is the target and the desired scattering object. In the second case, the bottom of the concrete is the desired target, and the rebar is clutter or the undesired scattering object.

A flat, smooth interface, relative to the wavelength, will scatter the incident wave energy without changing the energy shape (without changing the antenna pattern; Ulaby et al., 1982). This is known as specular reflection. As the interface becomes rough on the wavelength scale, the scattering becomes less specular and more diffuse. This is like going from a mirror to frosted glass, only on a larger

scale. In GPR, a typical example is a water table that appears rough with a thick capillary fringe in finer-grained materials or smooth with a thin capillary fringe in coarser materials. Another example is with gasoline or oil floating on the water table, changing surface tension and wettability to smooth the capillary fringe. If this occurs in a volume that is otherwise isotropic and homogeneous for energy propagating through it, the situation is like the difference between a frozen ice cube that is clear versus a snowball that looks white and translucent from light scattering. Such scattering creates wavelength- (or frequency-) dependent losses because the energy is not scattered in a useful direction, where "useful" means the energy comes back to the receiver. However, this frequency dependence becomes a diagnostic of the scale of the scatter objects (such as the capillary fringe or rocks buried as road fill), and the depolarization may indicate texture (paleoriver channels seen by space shuttle radar under sands in the western Sahara; Schaber et al., 1986).

GPR system and performance

GPR has been deployed from the surface by hand or vehicle towed, in or between boreholes or tunnels, from aircraft, from satellites, and between planets. It is sometimes used to look through walls, e.g., to detect people. GPR operates by emitting radiofrequency EM energy as a short-pulse or swept frequency from a transmitter antenna. The energy is coupled into the ground from the transmitting antenna, and some fraction of the energy returns to the same antenna (monostatic) or a separate receiving antenna (bistatic). The properties of the radar system determine what happens to the signal getting to the transmitter and back from the receiver; but between the transmitter and receiver antennas, it is controlled by the geometry of the antennas and the properties of the ground, including coupling and buried-object (target) responses. This latter is described by the radar equation, which in one form is (Noon et al., 1998)

$$G_{Tx}C_{Tx}G_{Rx}C_{Rx}P_S = \frac{(4\pi)^3 R^4}{\lambda \vartheta \exp(-4\alpha R)}, \qquad (6)$$

where the radar-system parameters are on the left-hand side and the ground and target parameters are on the right. The values G_{Tx}, C_{Tx}, G_{Rx}, C_{Rx}, and P_S are, respectively, the transmit and receive antennas' directional gains and coupling efficiencies and the radar-system performance (the ratio of mean transmitted power to the minimal detectable signal); α is attenuation in nepers/m; λ is wavelength in the ground; ϑ is the scattering target cross section; R is the distance to the target; $\exp(-\alpha R)$ represents two-way material attenuation losses; and R^4 is two-way geometric spreading loss (with an exponent that varies with target type; see Noon et al. [1998] for examples).

The radar system puts energy into the transmitter antenna at a specified power and frequency spectrum, expecting a certain impedance match going into the antenna. With most air-coupled antennas, this expectation is usually met; but with ground-coupled antennas, the properties of the ground may change the impedance match and the efficiency of the transmitter (the equivalent also occurs at the receiver) as the antennas move over changing ground conditions. This change of impedance match contains useful information. It is difficult to calibrate (Oden et al., 2008) for ground-coupled antennas but relatively easy to calibrate for air-coupled antennas against a surface that should be smooth and horizontal at the wavelength scale, such as pavement (Maser and Scullion, 1992). To use a GPR quantitatively, this is where we must start making assumptions (Olhoeft, 2000).

Horizontal and vertical resolutions are not the same for GPR, and they vary with position and depth. Both are a function of wavelength and geometry (including depth). The vertical resolution is a function of wavelength and scatterer size or layer thickness. It also depends on signal-to-noise ratio (S/N) and signal-to-clutter ratio. For pulse radars, the vertical resolution is generally one-third to one-fourth of the dominant wavelength with normal noise and clutter (Yilmaz, 2001; Daniels, 2004). For frequency-domain GPR, it is given in terms of the bandwidth used to determine the ability to distinguish between (resolve) two targets closely spaced in depth, and it is given as the propagation velocity divided by the square root of two times the bandwidth.

The Fresnel zone describes the circular region on an interface (or in an ellipsoidal volume for a scattering object) that coherently diffracts or backscatters energy and thereby specifies resolution (Smith, 1997; Yilmaz, 2001). The horizontal resolution is proportional to the square root of the product of wavelength and depth (Daniels, 2004). Wavelength should be understood as the wavelength in the ground, including pulse broadening with propagation distance. Horizontal resolution can be improved by migration, which is described later. Vertical resolution can sometimes be improved by deconvolution.

Common assumptions, limitations, and consequences

Many common assumptions are made in acquiring, processing, modeling, and interpreting GPR data. Each assumption has limitations with consequences that can lead to misinterpretation. The magnetic properties are often assumed to be those of vacuum or free space. Because the product of magnetic permeability and permittivity determines velocity, depth will not be compromised; but if the permittivity is then used to estimate water content, the water content will be too high. Using only electric-field antennas will not let the magnetic component be separated. If two high-contrast objects are buried on top of each other, the topmost will shadow the lower one, which can be dangerous when dealing with UXO. The geometry of reflection from the top and bottom of a hollow plastic pipe may look like two hyperbolas, misinterpreted as two separate objects. A syncline may appear, as in seismic pitfalls (Yilmaz, 2001), as a bow tie masquerading as an object hyperbola. Interpreting velocity from hyperbolas is dangerous when other processes create patterns similar to hyperbolas (such as ice melt in permafrost around a hot pipeline or reflections from overhead wires or nearby cars). Ignoring the antenna radiation pattern will not let geometric distortions be corrected properly. Ignoring antenna ground coupling will not give correct full-waveform modeling of details.

Although velocity can be measured by a variety of means (Olhoeft, 2000), it is often assumed based upon site conditions (measured in one location and assumed to be useful for the whole site). This is particularly dangerous with depth, such as above and below a water table where depth to a pipe using only one velocity will result in errors in depth estimates and increased excavation hazards. The same thing can happen horizontally if moving from concrete to soil changes not only velocity but also antenna coupling. With a multilayered earth, wave guides may appear along with multipathing and can create errors in horizontal and vertical positions (Sander et al., 1992). Because of the way most antennas work, they radiate the wavefield in a wide beam and see off to the side as well as forward and aft, allowing the possibility of out-of-plane scattering from objects not directly under the antenna traverse (Olhoeft, 1994). This is advantageous when 3D data are collected covering an area, but it can lead to pitfalls when interpreting 2D GPR data collected along a line. In that case, ignoring the out-of-plane possibility and fitting hyperbolas to the resultant shape will give the wrong velocity, depth, and location of the scattering object (it is a different cross section through a 3D hyperboloid). Errors are introduced in full-waveform amplitude modeling when air-launched antennas are calibrated on a sloped railroad ballast bed, assuming a horizontal surface, or on gravel beds that are rough at the wavelength scale, assuming it is smooth (Olhoeft et al., 2004).

BOREHOLE GPR

Borehole GPR operates in a single borehole, between two boreholes (crosshole GPR), from a borehole to the surface (vertical radar profile), or from a borehole to a mine tunnel. In each situation, the surrounding conditions of the antennas are very different from those of surface GPR antennas. Fundamental studies on the behavior of antennas in cylindrical structures, which can be used for designing borehole radar antennas, can be found in King and Smith (1981), Greenfield (1988), and Sato and Thierbach (1991). Schematics of a borehole radar measurement in single- and crosshole modes are shown in Figure 1. Because antennas in boreholes are strongly affected by the surrounding medium, the antenna characteristics are
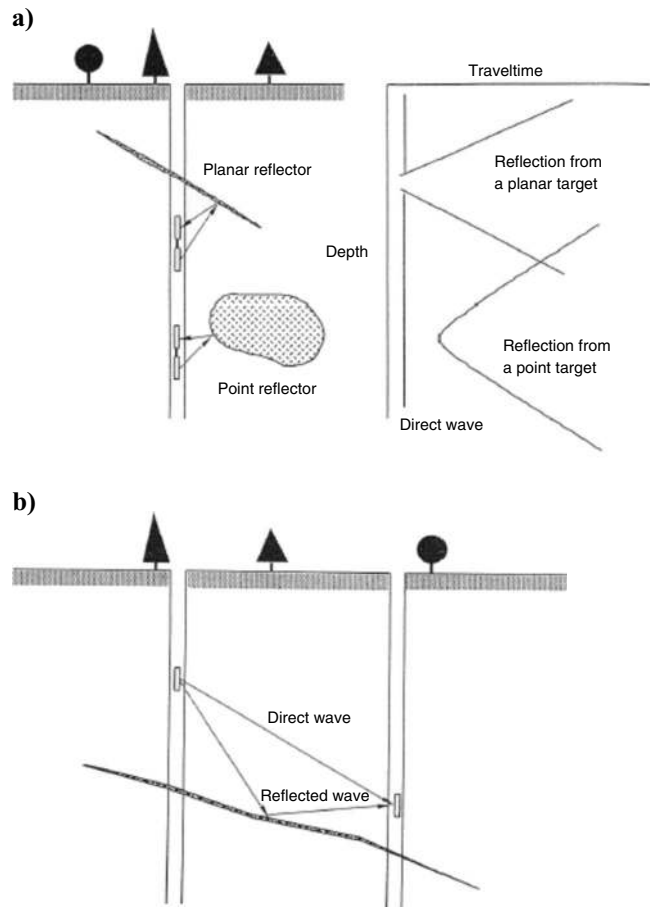

Figure 1. Schematic representation of borehole GPR measuring configurations. (a) Transmitter and receiver are set in the same borehole in single-hole measurement, whereas (b) in crosshole measurement, they are set in separated boreholes.

quite different from those in free space. The interaction of antennas and the surrounding materials is important for various applications, which is why antennas located in a dispersive medium have been studied in detail (Lytle and Laine, 1978; King and Smith, 1981; Scott and Chang, 1984).

The borehole-antenna radiation patterns and the received signal forms are important for understanding the radar system. Because the host rock is heterogeneous, the radiation patterns are difficult to measure in situ. For this reason, in the 1980s, people started modeling the antennas and theoretically analyzing borehole radar antennas. Semianalytical approaches (King and Smith, 1981) were used for understanding the transient behavior of borehole radar systems. This kind of analysis was followed by a full theoretical analysis of the transmitted and received waves in borehole conditions (e.g., Sato and Thierbach, 1991).

Borehole radar antennas are confined to the cylindrical shape of the borehole, and the radar system is incorporated in the same cylindrical structure as the antennas. Borehole radar must be used in boreholes that are filled with air or water, so the antennas and the borehole system are housed in a waterproof case. Furthermore, usually metallic wires transport the radar signal to the surface. The housing and wiring result in a radar system whose antennas exhibit very complicated radiation patterns, and these patterns are not easily modeled numerically. A direct consequence of the complicated radiation pattern is the fact that at high transmission angles, the wavefields are received at antenna positions away from the antenna feed points. This can lead to large errors in velocity estimates based on such arrivals because it is assumed they are recorded at the feed points (Irving and Knight, 2005).

Recent advances in computational capability have made it possible to analyze the radiation in realistic borehole conditions by using finite-difference time-domain (FDTD) analysis (Teixeira and Chew, 2000; Holliger and Bergman, 2002; Liu and Sato, 2005; Ernst et al., 2006; Irving and Knight, 2006). These realistic models include cy-
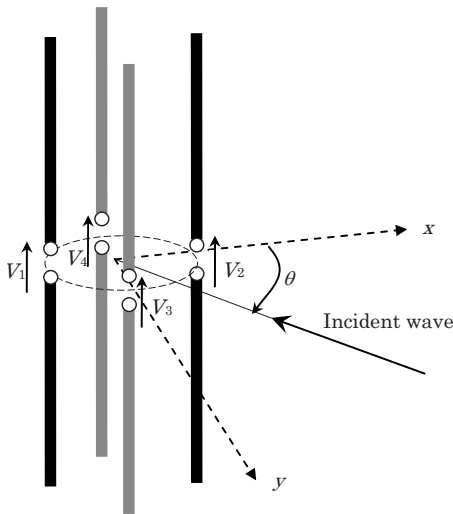

Figure 2. Orthogonal placement of four linear dipole antennas to form an antenna array for directional borehole radar; directionality is achieved by taking the difference in measured signals between antenna pairs. The phase difference among the received voltages (V_1, V_2, V_3, V_4) at each dipole antenna is used estimate the incident-wave azimuth angle θ.

lindrical geometries, general dispersive models, and proper representations of borehole antennas.

Physical limitations and challenges

Normally, few boreholes are available for measurements at a specific site, so we need to obtain as much subsurface information as possible from a single borehole. Consequently, we use lower frequencies compared to conventional surface-based GPR to achieve a larger penetration range. Most current borehole radar systems use frequencies below 100 MHz, which can achieve a penetration range of 20–50 m in crystalline rock, and up to 2000 m in salt. The diameter of boreholes available for borehole radar is usually less than 15 cm, so the outer diameter of the waterproof downhole tool containing the borehole radar is limited to this dimension. Most borehole radars use long, thin dipole antennas for transmitter and receiver because the geometric structure fits the shape of the thin tool. The diameter of the borehole is typically less than one-tenth of the wavelength of the radar signal. Therefore, the radiation pattern of most borehole radar antennas is considered omnidirectional around the borehole axis. These physical restrictions limit the borehole radar operations because we often want to know the 3D orientation of subsurface targets. Directional borehole radar antennas have been developed to meet this need (Lytle et al., 1979).

To achieve directivity using a thin borehole antenna, several approaches have been proposed. A dipole antenna with a reflector has a directional radiation pattern around the borehole axis. However, the antennas must be rotated mechanically, which makes the system complicated. This type of antenna can be used practically only when the diameter of the borehole is relatively large (van Dongen et al., 2002) because decreasing the separation between antenna and metallic reflector reduces antenna efficiency. An eccentric (off-center) location of a single dipole antenna can break the axial symmetry and achieve a directional radiation pattern without reducing antenna efficiency. However, the radiation pattern is still almost omnidirectional because the borehole diameter is usually much smaller than the dominant wavelength (Lytle and Laine, 1978).

Most directional borehole radar tools are equipped with a pair of Adcock antennas or crossed magnetic-loop antennas (Lytle and Laine, 1978; Eisenburger et al., 1993; Eisenburger and Gundelach, 1999). Orthogonal data sets can be acquired from these types of array antenna systems, and directivity of the system can be achieved by signal processing, such that mechanical rotation of the antenna is unnecessary. This type of directional borehole radar system is widely used in salt and crystalline rocks (Eisenburger and Gundelach, 2000).

Currently, an antenna array is the most common approach to achieve a directional radiation pattern in a thin borehole. An Adcock array (Adcock, 1959) composed of multiple parallel dipole antennas can measure the phase differences between antennas to achieve the desired signal directivity. Two orthogonal pairs of dipole antennas shown in Figure 2 are the basic configuration of the Adcock antenna. A simple signal processing algorithm (Olsson et al., 1992),

$$F(\theta) = F_1 \sin \theta + F_2 \cos \theta, \tag{7}$$

where

$$F_1 = V_1 - V_2, \quad F_2 = V_3 - V_4, \tag{8}$$

is used for direction finding. In equations 7 and 8, F_1 and F_2 are the difference signals constructed from the signals $V_1, V_2, V_3,$ and V_4 received by two orthogonal dipole antenna pairs (Flachenecker, 1978;

Olsson et al., 1992; Yi et al., 2005) or signals of a pair of orthogonal-loop antennas (Nickel et al., 1983). These antenna pairs can steer the direction angle θ of the maximum amplitude in the radiation pattern (equation 7) and estimate the direction of the arriving signal. This is a very common approach for achieving directivity in borehole radar, but the hardware system is complicated because it must have multiple antenna feeding systems or a switching circuit. A multichannel system is chosen here rather than rotating a single directional antenna.

Borehole radars that achieve directionality using multiple antennas suffer from mutual antenna coupling because the antennas are located very close to each other in a thin, cylindrical structure. These mutual couplings cause phase deformation, and direction-estimation accuracy can be reduced because of that. The electric components, such as amplifiers, must be located close to the antennas, which causes additional deformation of phase characteristics.

To avoid this problem, Sato and Takayama (2007) propose an array borehole radar system using an optical electric-field sensor. The amplitude of the optical signal transmitted through an optical fiber is modulated by the sensor, and the received signal is modulated by the sensor and transmitted into the optical fiber; then the radar signal can be recovered by an optical detector. Because this is a passive sensor, we do not need a power supply such as batteries, and the sensor is free from large, signal-distorting metal components. It makes the performance of the closely spaced antennas in the array much better than that of a conventional antenna array with active components such as preamplifiers.

Crosshole and single-hole borehole radar measurements have been conducted at the Kamishi test site, Japan. Figure 3a shows an example of a borehole radar profile measured by an omnidirectional antenna. From the single-hole radar data, we estimated the azimuth orientation of the subsurface fractures. A simple algorithm based on the synthesized rotating radiation pattern of the antenna array can be used to estimate azimuth orientation. Figure 3b shows the estimated azimuth angle of each scattered waveform recorded with the new directional array system using optical electric-field sensors. The algorithm to estimate the direction of the targets does not differ much from the conventional method, but we can see high-quality 3D orientation of subsurface fractures. By combining the new hardware and the azimuth-estimation software, we achieve an estimate of the reflected-wave azimuth angle with an accuracy of about 30°. The 3D orientation of the subsurface fractures could be estimated by this system, as demonstrated in single- and crosshole tests in Korea (Takayama and Sato, 2007).

Radar polarimetry

An EM wave has two orthogonal components spanning the plane perpendicular to the propagation direction. Radar polarimetry measures single and multiple polarizations at the same time. And radar polarimetry measures not only the amplitude of the scattered wave but also scattering mechanisms of targets. As noted earlier, EM waves are described by vector fields, and the components of these vectors contain information about the 3D objects that scatter the wave. Scattering can be described by Stokes' matrix, which is a 4 × 4 complex matrix; the radar cross section, which is used in conventional radar analysis, is only one real value out of this matrix. The scattering depends on the frequency bandwidth; therefore, we also must select the operation-frequency bandwidth. Wave propagation in material normally suffers from strong attenuation, and the operat-

ing frequency must be low. In these cases, the radar resolution is poor as a result of the limitation of the frequency bandwidth. However, by exploiting radar polarimetry, we can acquire geometric information about the scattering objects without high-resolution images of the targets.

Figure 4 shows an FDTD simulation of scattering from a subsurface fracture model with a rough surface. A vertical electric-dipole
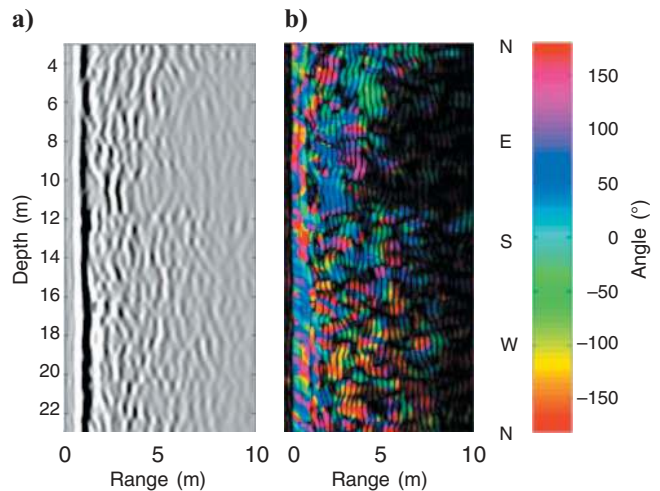
Figure 3. (a) Borehole radar profile acquired by an omnidirectional system. Azimuth information is missing; therefore, orientation information of each fracture is unavailable. (b) Directional borehole radar profile obtained by a system developed by Tohoku University (Sato and Takayama, 2007). Azimuth orientation of reflections is indicated by color; 3D fracture orientation information is available.
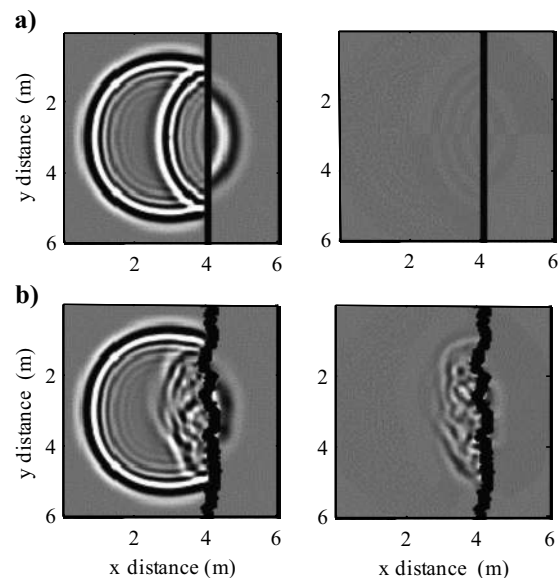
Figure 4. A 3D FDTD simulation of EM wave scattering from a subsurface fracture. A vertically polarized point source is placed at the center of the space. (a) Response from a thin fracture with a flat surface. (b) Response from a thin fracture with a rough surface. Figures in the left column show the vertically polarized wave, which has the same polarization as the incident wave. Figures in the right column show the horizontally polarized wave, which is cross-polarized to the incident wave. A flat surface causes a copolarized reflection wave only, but a rough surface causes co- and cross-polarized reflected waves.

point source is placed at the center of the space. The model in Figure 4a has a thin fracture with a flat surface, whereas the model in Figure 4b has a thick fracture with a rough surface. The plots on the left show the vertically polarized wave, which has the same polarization as the incident wave. The plots on the right show the horizontally polarized wave, which is cross-polarized relative to the incident-wave polarization. A flat surface causes only a copolarized reflected wave, but a rough surface causes co- and cross-polarized reflected waves. Without imaging the detailed structure, polarimetric radar data can be used to estimate fracture roughness, which is related to the hydraulic permeability of the fracture.

Many techniques have been proposed for analyzing polarimetric radar information; α-entropy classification is one such technique (Cloude and Pottier, 1997) that has been applied to polarimetric

borehole radar data. The angle α ranges from 0° to 90° and is a measure of the type of scattering. A zero angle means surface scattering in the geometric optics limit (specular reflection). The angle continuously increases for surface scattering under physical optics applied to the Bragg surface model, moves from dipole scattering into double bounces between dielectric objects, and finally ends in scatter from metallic surfaces at $\alpha = 90°$. Entropy, on the other hand, is a parameter interpreted as a measure of the randomness of a target's scattering mechanism, widely used in radar polarimetry in spaceborne and airborne remote sensing. Figure 5a shows four migrated polarimetric borehole radar profiles, and Figure 5b shows the plots of reflected waves on the α-entropy classification plane. Fractures at 28, 40, 47, and 55 m are located in different parts of the α-entropy classification plane. This is because of different scattering mechanisms occurring at the different fractures, and the information can be used for fracture characterization. Details of this analysis can be found in Zhao and Sato (2006).

Crosshole data imaging and inversion

Tomographic techniques are among the most popular imaging schemes used for crosshole geophysical measurements. If the host rock contains fractures and if these are saturated with water, macroscopic electric permittivity increases and thus the EM-wave velocity decreases and the attenuation increases. Using these properties in analyzing crosshole borehole radar, velocity, and attenuation tomography has been successful for imaging fractured or water-permeable zones where macroscopic changes of the electrical properties of the host rock are caused by water penetration. Compared to the size of targets such as subsurface fractures, which can have an aperture of only a few millimeters, the wavelengths are too long to image the structure in detail. Therefore, crosshole radar tomography on fracture zones creates images of anomalous zones that are much larger than the targets. For these applications, we are interested in imaging approaches as alternatives to tomography that can be applied to crosshole borehole radar data (Zhou and Sato, 2004; Takahashi and Sato, 2006). If the host rock is relatively resistive, EM attenuation is small and signal-processing techniques used in seismic signal processing are quite useful for borehole radar. Zhou and Sato (2004) test applying a scalar migration scheme to crosshole radar data acquired for air-filled cavity detection. The borehole separation was 20 m, and the depth of the cavity was more than 70 m.

Figure 6a shows a velocity tomography result applied to the crosshole radar data sets, based only on the first-arrival time. The high-velocity region corresponds roughly to the location of the air-filled cavity, but its area is about 10×5 m and the boundary is unclear. Then reverse-time migration is applied to the same data set using the full waveform, and the image shown in Figure 6b
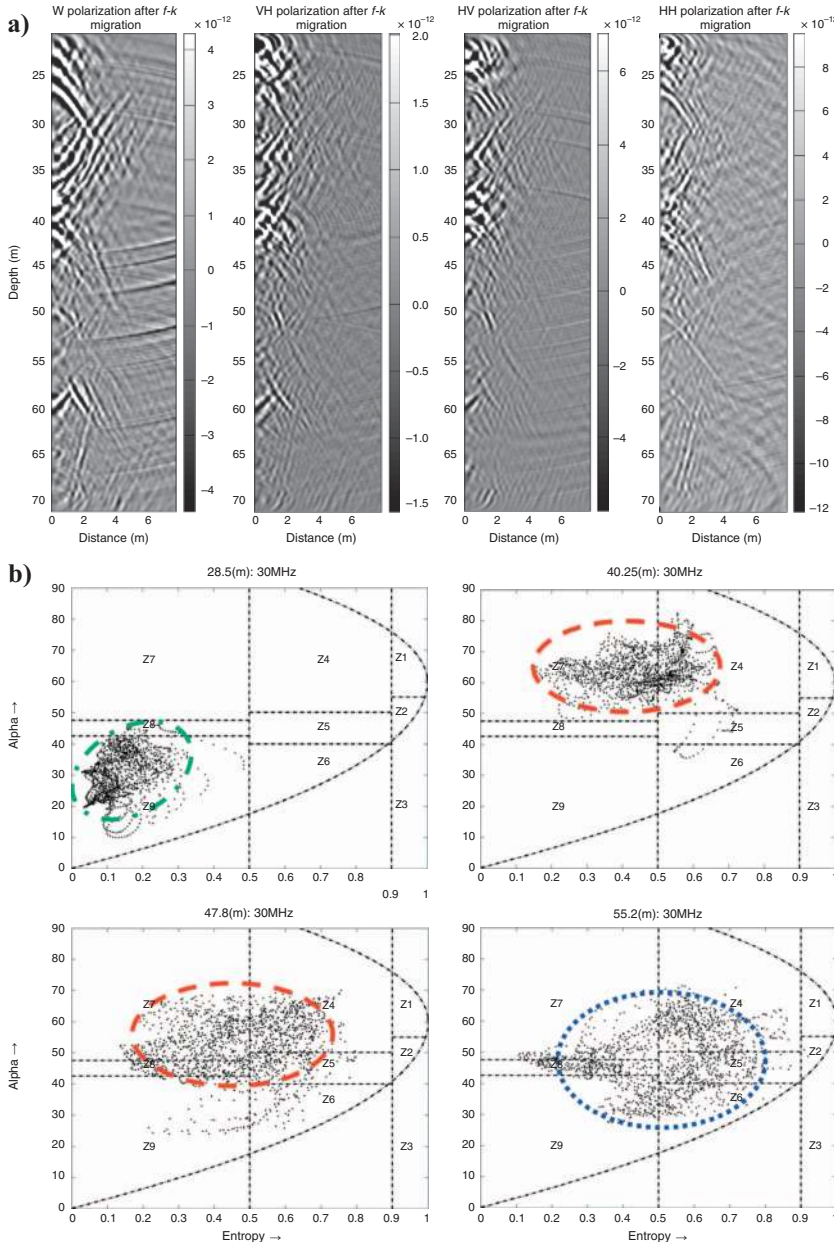

Figure 5. (a) Polarimetric borehole radar profiles of subsurface fractures. (b) Plots of α as a function of entropy for the four reflected signals at four different depths of the VV-polarized radar profile in (a).

is obtained. The anomalous area is much better focused than that in Figure 6a. The actual target in this site is an air-filled cylindrical cavity whose diameter is about 3 m. At this relatively large scale, we could image the air-filled cavity by reverse-time migration. Another example of velocity, attenuation, dispersion (from frequency-dependent scattering), and diffraction (migration) tomography is found in Olhoeft (1993).

IMAGING SURFACE GPR DATA

Ground-coupled antennas

To detect subsurface objects in GPR data collected at the surface, it is usually sufficient to measure and interpret the data in real time. If the objects are small, weak scattering objects that are close to the surface, the background field needs to be subtracted. In addition, it pays to correct for time-zero drift and to filter out low frequencies. This can all be done in real time, and data acquisition can be carried out in the fastest possible way. In the data, the presence of small objects is observed as diffractions that look like hyperbolas. They are easily visible even with only crude knowledge of antenna positions during the survey.

To detect and localize subsurface objects, their position in space must be estimated from the data. Depth information can be retrieved when reflection arrival times can be determined from the data. A depth estimate can be obtained when an effective velocity between the surface and the scattering object is known. This velocity can be estimated from the diffraction pattern in fixed-offset GPR data when it is clearly visible in the data and the object is present in an approximately homogeneous embedding. If the velocity estimation is hampered by fixed-offset data quality because the object cannot be considered small compared to the dominant wavelength or because of weak scattering, velocity profiles should be obtained from multiple offset data (common-midpoint gathers, or CMPs) or from running several imaging procedures using different velocities. The first option slows the acquisition operation because multichannel systems are uncommon; for the second option, knowledge of the antenna positions is of paramount importance.

For the Apollo 17 lunar rover, real-time positioning and antenna orientation were realized and built, but the technology remained classified for years (see, e.g., Simmons et al., 1972; Jones and Glover, 2007). In the public domain, Lehmann and Green (1999) were the first to demonstrate the possibility of real-time antenna-position measurements during GPR surveys. They used a laser-tracking theodolite in combination with a low-frequency antenna system and argued that improved acquisition speed was the major advantage. Lehmann and Green (2000) implemented topographic migration using antenna-position information in three dimensions. Since then, Slob et al. (2003b) have demonstrated that high accuracy in antenna-position information drastically reduces the clutter in resulting images compared to manually collected data. Grasmueck et al. (2005) demonstrate the usefulness of densely sampled GPR data for their ability to construct high-quality images from single-component data. They conclude that the bottleneck for applications requiring high-resolution images is acquisition time, not data-processing and migration time. The combination of acquiring densely sampled GPR data along with high-accuracy antenna information is used by Grasmueck and Viggiano (2007), who develop a real-time local laser-guided positioning system to work with GPR. Global-positioning-system (GPS) coordinates can also be measured in real time, and most commercial GPR equipment offers this option.

In all of these efforts, traveltime information is exploited in standard scalar imaging techniques (e.g., Gazdag, 1978; Stolt, 1978; Curlander and McDonough, 1991; Fisher et al., 1992b). Essentially, only arrival time, or phase, information is exploited; amplitude decay or radiation patterns of the antennas used are not properly accounted for. These standard scalar imaging techniques are known as phase-shift migration, synthetic aperture radar (SAR), diffraction stack, and Kirchhoff migration.

In cases where the scattering amplitudes are small compared to the direct waves or interface reflections, or when the shape of the scattering object becomes of vital importance, as in buried antipersonnel land mines, it is important to have high fidelity in antenna location and orientation information, antenna directivity, and subsurface wave velocity distribution. This indicates the need for full polarimetric imaging procedures that account for radiation patterns of sources and receivers, for radiated source-time signature, and for propagation loss. A forward model describing these factors can be represented as

$$E_{\alpha\beta}^s(\mathbf{x}^{\mathrm{Rx}}, \mathbf{x}^{\mathrm{Tx}}, \omega) \approx \int_{\mathbf{x} \in D^{SC}} D_{\alpha\beta}(\mathbf{x}^{\mathrm{Rx}}, \mathbf{x}^{\mathrm{Tx}}, \mathbf{x}, \omega) \chi(\mathbf{x}) \mathrm{d}^3\mathbf{x}, \quad (9)$$

where $\mathbf{x}^{\mathrm{Tx}}$, $\mathbf{x}^{\mathrm{Rx}}$, and $\mathbf{x}$ are the position vectors corresponding to the transmitter, receiver, and scattering locations, respectively. Equation 9 contains an approximately equals sign because the Born approximation for scattering is used, the antennas are assumed to be point devices, and scattering is assumed independent of frequency. The left side represents preprocessed data, where the direct field has been removed. The integration runs over the whole subsurface, and a practical limit is obtained from the survey area and the depth range that can be estimated from the time window of the measurement with a pulse GPR or the frequency bandwidth that has been used for a frequency-domain GPR. The subscripts α and β represent the orientation of the receiving and the transmitting antennas, respectively. The two-way wavefield extrapolator is denoted as $D_{\alpha\beta}(\mathbf{x}^{\mathrm{Rx}}, \mathbf{x}^{\mathrm{Tx}}, \mathbf{x}, \omega)$ (see Streich and van der Kruk [2007] for details), and the subsurface-electric-property function to be imaged is $\chi(\mathbf{x})$. The antenna positions, radiation patterns, source-time signature, and propagation-loss factors are incorporated in the two-way wavefield extrapolator D and are assumed known. The scattered electric field and the two-way wavefield extrapolator are a 2×2 matrix for every source-re-
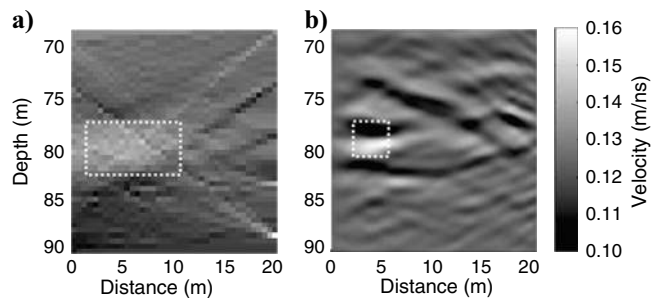

Figure 6. (a) Traveltime tomography result where the air-filled cavity appears as a high-velocity zone whose velocity is about 0.15 m/ns and is surrounded by a dotted square but the shape is unclear. (b) Reverse-time-migration result using the same data (Zhou and Sato, 2004). There are two strong events located at about (2–5 m, 78.5 m) and (2–5 m, 81.5 m). We interpret these to be the top and bottom of a cavity. The estimated position matches well with the true position of the cavity.

ceiver location, representing the horizontal electric vector field generated by two horizontal components of the source antennas.

Equation 9 therefore represents four equations. Figure 7 is a graphical representation of the *xx*-component of equation 9. Each scalar two-way wavefield extrapolator, mathematically expressed as $D_{11}(\mathbf{x}^{\mathrm{Rx}},\mathbf{x}^{\mathrm{Tx}},\mathbf{x}) = G_{k1}^{\uparrow}(\mathbf{x}^{\mathrm{Rx}},\mathbf{x})G_{k1}^{\downarrow}(\mathbf{x},\mathbf{x}^{\mathrm{Tx}})J_1$, is the inner product of two vector Green's functions that describe all radiation, propagation, and damping effects on the path from antenna to scattering object, and J is the source-time signature, as indicated in Figure 7.

First steps to full polarimetric migration were taken by Lehmann et al. (2000), who collected dual-component data and summed the two recorded data sets. This is similar to reducing equation 9 to a single equation:

$$E_{11}^s(\mathbf{x}^{\mathrm{Rx}},\mathbf{x}^{\mathrm{Tx}}) + E_{22}^s(\mathbf{x}^{\mathrm{Rx}},\mathbf{x}^{\mathrm{Tx}}) = \int\limits_{\mathbf{x}\in D^{SC}} [D_{11}(\mathbf{x}^{\mathrm{Rx}},\mathbf{x}^{\mathrm{Tx}},\mathbf{x})$$
$$+ D_{22}(\mathbf{x}^{\mathrm{Rx}},\mathbf{x}^{\mathrm{Tx}},\mathbf{x})]\chi(\mathbf{x})\mathrm{d}^3\mathbf{x}.$$
(10)

The summed data were then migrated with a standard scalar Kirchhoff migration scheme. Single-component vector-imaging algorithms were developed by Hansen and Johansen (2000). They introduced far-field radiation patterns (Engheta et al., 1982; Smith 1984) to avoid the numerically expensive incorporation of the earth surface and showed 2.5D and 3D results. Almost at the same time, Wang and Oristaglio (2000) introduced a similar algorithm based on the far-field approximation and the generalized Radon transform, which is a propagating plane-wave expansion. They found that the simultaneous reconstruction of permittivity and conductivity contrasts was difficult, and they separated the imaging problem in essentially imaging-permittivity contrasts or essentially conductivity contrasts. Later, van der Kruk et al. (2003) collected and imaged all four components of the data matrix of equation 9 using far-field expressions of the EM field propagating in a homogeneous half-space without correcting for the radiated source-time signature.

These far-field expressions are often used to describe EM wave propagation. However, comparison with the exact field shows that at a distance of 8λ, a significant error remains present close to the critical angle. Using the far-field radiation patterns in the two-way wavefield extrapolator to correct for the real radiation patterns is inadequate and leads to suboptimally focused images.

Correcting for the exact-field radiation patterns was accomplished later by Streich and van der Kruk (2007), who realized that the two-way wavefield extrapolator could be evaluated efficiently as soon as the waves are calculated below the earth surface and a wave-
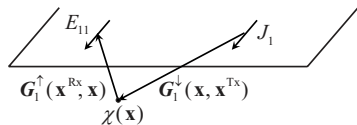
field extrapolator in a homogeneous space (phase shift in horizontal wavenumber domain) could be used to calculate the electric field at greater depths (Slob et al., 2003a). Only the first step — computing the two-wavefield extrapolator just below the earth's surface — is numerically expensive. This is solved empirically using a fast Fourier transform (FFT) and determining the necessary oversampling on the fly. Depending on acquisition configuration and medium parameters, this approach may lead to significant errors when used unsupervised. Such errors can be avoided by checking the resulting wavefield extrapolation operator for errors, at the cost of human intervention.

These phase shifts can be implemented for velocity functions varying smoothly with depth. For a generally heterogeneous subsurface and for horizontally directional subsurface objects such as pipes and cables, this is the best migration scheme available, but improvements are possible. It comes at the cost of acquiring four data sets in each survey or two data sets when only one polarimetric image suffices. Processing and migrating the data matrix is only marginally more expensive than migrating single-offset data, compared to the extra cost of acquisition. To detect or characterize objects independent of polarization, not all components have to be recorded (Streich et al., 2007). This applies to subsurface objects that are small or large compared to the dominant wavelength in the horizontal directions, such as small objects and reflecting boundaries. Single-component line data can be migrated using a 2.5D implementation of the single-component vector migration scheme (Orlando and Slob, 2009). Orlando and Slob (2009) show that subsurface directional structures (concrete rebars and subsurface elongated fractures) parallel to the main antenna polarization can be imaged accurately.

Radiation patterns of physical antennas will be different from the idealized point devices used in present-day schemes. Early attempts at modeling radiation patterns can be found in Arcone (1995) and Holliger and Bergmann (1998). Recent advances in the ability to model antennas in contact with the ground can be found in Warren and Giannopoulos (2009). The antenna/ground interaction filters require knowledge of the electric properties of the ground and filling material of the antennas as well as antenna geometry. When the antenna behavior depends strongly on ground impedance, this approach is impractical. An alternative to imaging using multicomponent data can be to simplify the receiver and transmitter functions and to replace them with a few equivalent point sources, each with an unknown and frequency-dependent scaling factor. These unknown coefficients can then be found with the aid of calibration measurements (Lambot et al., 2010).

Another approach to imaging using multicomponent data is provided by van Gestel and Stoffa (2001), who use Alford rotation to obtain direct information about a subsurface object orientation in the horizontal plane. They apply the far-field approximation for the radiation pattern and conclude that results might improve by using more accurate radiation patterns. Given the developments on radiation patterns during the last 10 years, this approach seems of interest to investigate.

Figure 7. Schematic representation of the model for multicomponent total-field imaging. The source J_1 emits an EM wavefield described by a two half-space Green's function $\mathbf{G}_1^{\downarrow}$ that brings the wavefield from the source to any location in the subsurface. When the wavefield encounters a scattering object with scattering strength χ, a secondary wavefield is emitted from the scattering object described by a similar Green's function $\mathbf{G}_1^{\uparrow}$ that brings the scattered wavefield to the surface where it is measured as an electric field E_{11} at the surface.

Air-launched antennas and accounting for antenna effects

To circumvent problems with antenna impedance matching the ground, air-launched antennas can be used. When they are at sufficient height above the ground, the electric field that is emitted can be regarded as independent from the subsurface. The horizontal com-

ponents of the electric field can be measured in a plane below the transmitting antenna. Knowledge of the horizontal electric-field components is sufficient to describe the downgoing wavefield. This measured downgoing wavefield can be extrapolated to larger depths, and the air/ground interface can be taken into account properly (Slob et al., 2003a). Once the downgoing wavefield below the surface is known, simple phase shifts in the horizontal-wavenumber domain establish further downward extrapolation. By reciprocity, the upgoing wavefield can be extrapolated using the same filters. Having the measured downgoing electric wavefield allows for multicomponent migration of the data matrix of equation 9, yielding high-resolution subsurface images (Bloemenkamp and Slob, 2003a). One advantage of this approach is that the antennas do not need to be included in the model because their effect is measured in the downgoing wavefield measurements. A second advantage is that the source-time signature is also part of the measured downgoing wavefield. In the multicomponent migration scheme, the antenna effects and the source-time signature are eliminated because the scheme is a linear-inversion algorithm with an imaging condition. This has proved beneficial in surface-laid and shallow subsurface buried antipersonnel land-mine detection and characterization efforts. Similar results are obtained by van Dongen et al. (2004) using a scalar approach on spiral antenna data. The benefit of using measured radiation patterns rather than computed patterns is that no model of the antennas is necessary and therefore the point-device assumption is absent. Spiral antenna data can be very well focused using scalar imaging algorithms, even for ground-coupled antennas. An example is given in the case history section.

Bloemenkamp and Slob (2003b) show how elevation of antennas affects the data. They observe that for vertical two-way travel distances smaller than one-third of the dominant wavelength, the deterioration is small. For larger distances, the effect increases rapidly. When the vertical two-way travel distance from antenna to surface is four-thirds of the dominant wavelength or more, the S/N is decreased, hyperbolic moveout of scattered events becomes flat, and the side-looking ability is reduced. These last two aspects occur because a larger part of the total travel path occurs in the air, which is the fast medium, and rays are bent toward the vertical axis for waves that penetrate the subsurface. Because the earth's surface is a strong reflector and the side-looking ability is reduced, the general applicability for object detection and characterization is decreased, for which ground-coupled antennas are desirable.

For surface and near-surface applications, these two aspects can be used advantageously by assuming a 1D earth model and monostatic mode of acquisition, where a single antenna is used as transmitter and receiver (Lopera et al., 2007). The 1D model in combination with monostatic radar allows for removing antenna effects by a simple calibration procedure. The antenna is assumed to be connected to the radar by a coaxial transmission line, and it is positioned in the far field of the surface. In that case, the antenna can be approximated by an independent yet interactive point source that can be characterized by its scattering parameters, as depicted in Figure 8. The full scattering matrix consists of four terms: the reflection and transmission coefficients from both sides of the antenna. When a unit amplitude signal enters the antenna at the input side, the antenna will partially reflect (represented by S_{11}^{ant}) and transmit (represented by S_{12}^{ant}) the incoming signal when there are no other scattering domains. Similarly, when a unit amplitude signal enters the antenna at the opening where it would act as a receiving antenna, the antenna will

partially reflect (represented by S_{22}^{ant}) and transmit (represented by S_{21}^{ant}) the incoming signal when there are no other scattering domains. Only the product $S_{12}^{ant}S_{21}^{ant}$ needs to be known for reflection measurements, and it is given by $H = S_{12}^{ant}S_{21}^{ant}$. The earth is assumed to be below the antenna, and its reflection response to a unit amplitude incoming wave is the earth impulse reflection response $G_{xx}^{\uparrow}$. When the antenna is located above the earth, the antenna and earth interact as represented in the rightmost diagram. The result is a feedback system that is described mathematically by a linear fractional transformation (Redheffer, 1961):

$$S_{11} = S_{11}^{ant} + \frac{HG_{xx}^{\uparrow}}{1 + S_{22}^{ant}G_{xx}^{\uparrow}}. \qquad (11)$$

Details of equation 11 and the implementation of the layered-earth reflection response can be found in Lambot et al. (2004b).

The true earth reflection response is obtained from equation 11 after the three antenna-scattering parameters are determined. This is achieved by performing several independent measurements with a known earth-reflection response, e.g., a perfectly electric conductor, for different antenna heights. Equation 11 has been used successfully in many studies to determine water-content depth profiles (Lambot et al., 2004a) and surface soil water content (Lambot et al., 2008) and to monitor water flow in an infiltration experiment (Lambot et al., 2009). All of these results have been obtained through full-waveform inverse modeling. A similar calibration approach for impulse radars is used by Chanzy et al. (1996), where the calibration is carried out by dividing the peak-to-peak amplitude of the measurement by the peak-to-peak amplitude of a measurement above a metallic plate at the same height. This surface-reflection method (Maser and Scullion, 1992) is used for estimating surface soil water content (Redman et al., 2002; Serbin and Or, 2003, 2004). A good overview
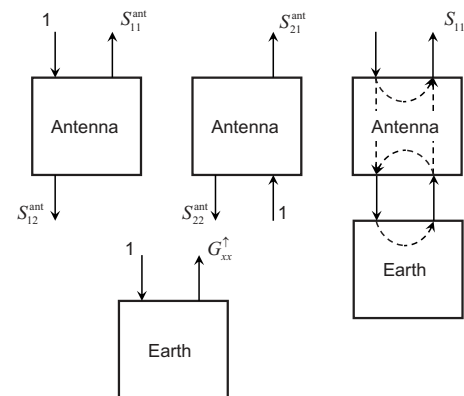

Figure 8. A graphic S-port representation of an off-ground antenna. When a unit-amplitude signal enters the antenna at the input side, the antenna will partially reflect (represented by S_{11}^{ant}) and transmit (represented by S_{12}^{ant}) the incoming signal when there are no other scattering domains. Similarly, when a unit-amplitude signal enters the antenna at the opening where it would act as a receiving antenna, the antenna will partially reflect (represented by S_{22}^{ant}) and transmit (represented by S_{21}^{ant}) the incoming signal when there are no other scattering domains. The earth is assumed to be below the antenna, and its reflection response to a unit-amplitude incoming wave is the earth impulse reflection response $G_{xx}^{\uparrow}$. When the antenna is located above the earth, they interact as represented in the rightmost drawing. The result is a feedback system that is mathematically described by a linear fractional transformation as given in equation 11.

on GPR techniques for measuring soil water content can be found in Huisman et al. (2003).

GPR IN HUMANITARIAN DEMINING: A CASE HISTORY

GPR and dual sensors for humanitarian demining

The United Nations estimates that more than 100,000,000 land mines remain buried in over 60 countries (Baum, 1998). Humanitarian demining is a very important and urgent issue not only in mine-affected countries but all over the world. A metal detector, which is an electromagnetic-induction (EMI) or eddy-current sensor, operating at 10–50 kHz has been widely used for humanitarian demining. These metal detectors can detect metal pieces weighing less than 10 mg contained in plastic antipersonnel mines located down to 20 cm below the surface. Therefore, these metal detectors can find almost 100% of buried land mines.

The high sensitivity of the device causes it to detect all kinds of small metallic objects. In a former battlefield, statistically only one out of 1000 metal objects detected by a metal detector is a buried landmine. This large number of metal fragments increases the cost of humanitarian demining operations. To improve the efficiency of the demining operations, the ability to discriminate land mines from other metal fragments is the most important capability an additional sensor should have.

Sensor fusion is a common way to increase the reliability of sensing capabilities. Hand-held sensors are more effective in small mine fields than vehicle-operated systems. For a handheld system, the sensor must be compact. However, because of very strong clutter from the ground surface and inhomogeneous soil in the GPR data, the combined use of GPR with a metal detector is advantageous. This dual-sensor combination is valuable for humanitarian demining. Only a few dual sensor systems have been commercially available since 2009; these include Mine Hounds (U. K. and Germany; Daniels et al., 2005), HSTAMIDS (U.S.A.; Doheny et al., 2005), Cy-Terra AN/PSS-14 (U.S.A.), and the advanced landmine imaging system, or ALIS (Japan; Sato, 2005). ALIS, developed at Tohoku University, Japan, has been deployed in real mine fields since 2009.

Handheld GPR system

ALIS has a few unique features that other dual sensors do not have. One of them is a sensor-position tracking system that can provide 3D GPR images and helps us understand the subsurface condi-
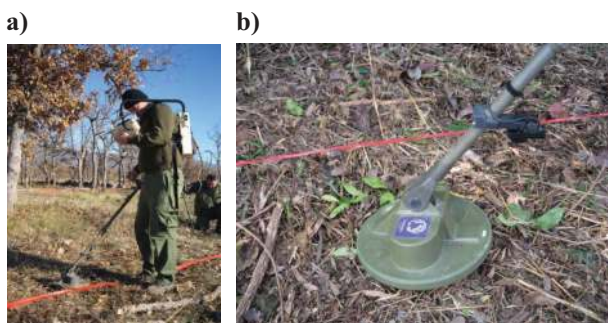
a)   **b)**

Figure 9. (a) Advanced land-mine imaging system (ALIS) in operation in Croatia with the CCD camera visible on the handle. (b) ALIS sensor head of cavity-back spiral antennas for GPR, combined with coils for an EMI (metal detector) sensor.

tions much better than conventional audio signals. It leads to a greater efficiency of detecting buried land mines (see Figure 9a).

ALIS has two different types of GPR hardware: stepped-frequency continuous-wave (SFCW) radar and impulse radar (Sato et al., 2007). The SFCW radar system for ALIS was achieved using a compact handheld vector network analyzer (VNA), developed by Tohoku University. The developed VNA measures $30 \times 20 \times 8$ cm and weighs less than 1.7 kg. Generally, a VNA combines a synthesizer and a synchronized receiver. It is controlled by a central processing unit (CPU) and can store the measured data in its memory. The calibration data can also be stored in the memory of the VNA, and the output data can be calibrated by using the stored data. This calibration function improves signal quality because it suppresses the reflection from antennas and any discontinuities caused by feeding circuits. ALIS-PG, an alternative of ALIS, is operated by using an impulse radar system. This impulse GPR system generates a short pulse of approximately 200 ps, which covers frequencies ranging from virtual DC to a few gigahertz. The radar signal is downsampled to an audio signal for further signal processing and recording.

One of the advantages of a VNA GPR system compared to the impulse GPR is its flexibility in selecting the operation-frequency range. The impulse duration of the impulse GPR is normally fixed, and we cannot change the operation frequency depending on soil conditions. However, the important advantages of an impulse GPR system are its light weight and fast data-acquisition rate. We conclude that, for relatively dry soil and shallower targets such as land mines, an impulse GPR system is easier to operate and can provide satisfactory results, whereas VNA GPR has advantages in wet soil and for deeper targets. However, these technical issues are strongly hardware dependent, especially the S/N of each electrical component. In theory, there is no difference between SFCW and impulse radar systems, but in practice there is.

Figure 9b shows the ALIS sensor head. ALIS uses cavity-back spiral antennas for transmitter and receiver. This type of antenna is selected for its good performance in a wide frequency range and the high isolation between transmitter and receiver antennas because they are closely spaced in the sensor head. In addition, circular polarization is suitable for detecting targets with unknown orientations. The antennas are combined in the sensor head with a coil sensor acting as the metal detector. The locations of coil and antennas are optimized to avoid mutual interference. The metal detector that we used for ALIS has differential receiving coils. Therefore, it is insensitive to metal objects that are placed symmetrically to the metal detector coils. As a direct consequence, the metal detector is not affected by cavity-slot antennas used for GPR. The EM wave from GPR is transmitted through the coils of the metal detector, and it has some influences; but we have found that the reflection from the coils can be suppressed by signal processing.

Sensor-tracking system

The most unique feature of ALIS is its sensor-tracking function. During operation, the sensor operator can observe the metal-detector-response image along with a picture of the ground surface on a display. Signal processing requires antenna-position information, and GPR imaging is impossible in conventional handheld GPR and dual sensors because the trajectory of the sensor is unknown in a handheld system. ALIS uses a CCD camera fixed on the handle of the sensor head for sensor tracking, which can be found on the handle shown in Figure 9a. The charge-coupled device (CCD) camera

captures images of the ground surface, the relative movement on the ground surface is calculated by a crosscorrelation algorithm, and the sensor position can be tracked (Doerksen, 2002). Figure 10a shows an example of the tracked sensor position. The dots indicate the positions where ALIS acquired GPR and metal-detector data along with the sensor positions.

Imaging

As discussed, one of the advantages of GPR is the ease of understanding and interpreting acquired data sets. On many occasions, the location of the buried objects can be observed directly in GPR profiles. Unfortunately, buried antipersonnel mines are very difficult to detect in GPR data because of strong clutter. Figure 10b shows an example of a raw GPR horizontal slice acquired in a mine field in Cambodia. We know that an antipersonnel mine is buried in this area; however, strong clutter masks the image of a buried mine. In this particular location, soil does not contain gravel or other solid objects; therefore, this GPR image principally represents moisture heterogeneity. We can define clutter as radar signals reflected from objects that are not our targets. Clutter is caused mostly by strong heterogeneity in the soil. Small buried materials such as soil grains, grass roots, different geologic materials, and inhomogeneous soil moisture cause this electrical heterogeneity in the soil. The antipersonnel-mine size is close to the scale of heterogeneity, although many civil or environmental targets such as buried pipes are larger or smaller. The importance of signal processing in GPR for detecting land mines has been overlooked in many test pits where homogeneous sands were used as filling material and clutter was negligible.

The GPR data acquired with the sensor-position information are processed after scanning the ALIS sensor over an area of about 1 $\times$ 1 m. We construct a 3D GPR image by Kirchhoff migration. The resulting 3D migration image can be interpreted with the scan result of the metal detector. The metal detector result is shown in Figure 11a, and the corresponding depth slice from a 3D GPR image is shown in Figure 11b. We find that a horizontal slice through the image volume (Figure 11b) is very useful for data interpretation in field situations. The PMN-2, an antipersonnel land mine produced in the former Soviet Union, is the target in these GPR profiles. Figure 10b is a time slice of the raw data, whereas Figure 11b is a depth slice after 3D migration; the figures cannot be compared directly. However, we can observe that migration has drastically increased the quality of the GPR image.

Figure 12 shows the radargrams of one of the scanning lines in Figure 10a. Figure 12a is the raw data, and Figure 12b is the Kirchhoff migration image. We can find no obvious improvement in these radargrams, but the depth slice is drastically improved in Figure 11b. We think the vertical heterogeneity is very strong in this soil; therefore, we cannot find the buried-target image in the radargram. This seems to be a typical soil condition for real mine fields, and the importance of imaging can be understood. The operator will interpret both the metal-detector image of Figure 11a and GPR images on the PC display as we see in Figures 11b and 12; then the operator will judge the types of buried objects from these two images.

Evaluation tests in mine-affected countries

International organizations such as the International Test and Evaluation Program for Humanitarian Demining (ITEP) are conducting sensor evaluation tests for humanitarian demining under controlled conditions. They also provide technical information on tested sensors to end users. ALIS has been tested in some mine-affected countries, including Afghanistan (Sato, 2005), Egypt, Croatia (Sato, 2009), and Cambodia. Mine fields in each country have different conditions and soil types, which is why tests in real mine fields are very important.

After a six-month test in Croatia, where ALIS was used in real mine fields for quality control, two sets of ALIS instruments were introduced in real mine fields near Siem Reap, Cambodia, in May 2009. In July 2009, an operation was carried out in collaboration with the Cambodian Mine Action Center (CMAC). In a 4192–m² area, 1193 buried objects were found using two ALIS instruments (see Figure 12 for one of the data sets). Nine of these objects were mines, all PMN-2. The metal detector found 1193 objects; but with ALIS, the deminers were able to judge 484 of them as possible mines and 709 as metal fragments. This meant that 709 out of 1193 points (about 60%) did not have to be prodded, reducing the time of demining operations drastically. This is the most important contribution of GPR, and ALIS in particular, to reducing the antipersonnel landmine problem.

PRESENT AND FUTURE DEVELOPMENTS

The international regulatory environment

For many years, GPR could be used without specific limitations enforced by governments. GPR is now regulated in parts of the world as an ultrawide-band (UWB) device (Taylor, 1995; Olhoeft, 1999; Paulino et al., 2008) with specific power, frequency, and usage limitations. Regulatory offices are the U. S. Federal Communications Commission (FCC) and the European Telecommunications Standards Institute (ETSI). Their standards can be found as FCC 47 CFR Part 15 subpart F and ETSI TR 102 554 v1.1.1. In the United States, the FCC defines GPR as "A field disturbance sensor that is designed to operate only when in contact with, or within one meter of, the ground for the purpose of detecting or obtaining the images of buried objects or determining the physical properties within the ground. The energy from the GPR is intentionally directed down into
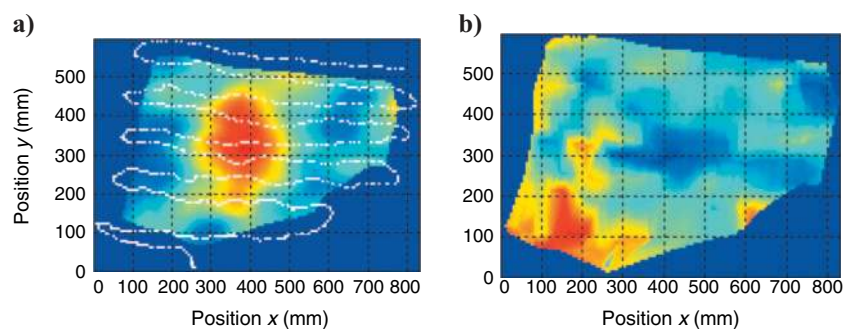

Figure 10. (a) GPR depth slice and locus of sensor position; each dot indicates where GPR and metal-detector signals are acquired. (b) Time slice of the raw data; a PMN-2 is located at the center of this area, but strong clutter from the soil shades the image.

the ground for this purpose" [c15.503(f)] (Federal Communications Commission, 1996). This implies that airborne GPR is not considered ground-penetrating radar according to the regulators in the United States and requires a special permit.

Modeling, tomography, and full-waveform inversion methods

With increased computer power, it has become standard to run numerical 3D models for many different GPR applications (e.g., Teixeira et al., 1998). A free FDTD-based simulation package (Giannopoulos, 2005) can be found at http://www.gprmax.org. Current FDTD provides full-value GPR modeling tools. Modern implementations include the possibility of modeling realistic antennas (Lampe et al., 2003; Warren and Giannopoulos, 2009) and magnetic losses in the materials (Cassidy and Millington, 2009). Large 3D models can be computed because the domain of computation can be kept small using perfectly matched layers as boundary conditions (Giannopoulos, 2008) and using subgridding to incorporate fractures or other small-scale model features (Diamanti and Giannopoulos, 2009). A review of practical simulation methods for GPR applications in near-surface environments can be found in Cassidy (2007).

Tomographic and full-waveform inversion methods have been developed as a general tool for inverting GPR scattering data for a variety of applications, including subsurface water-content estimation (Bradford et al., 2009; Irving et al., 2009; Crocco et al., 2010; Minet et al., 2010) as well as methods using properties of waveguides for inverting near-surface properties (Arcone et al., 2003; Strobbia and Cassiani, 2007; van der Kruk et al., 2007; van der Kruk et al., 2009). Multioffset data have been used in AVO inversion to estimate thin-bed properties (e.g., Deparis and Garambois, 2009). Borehole GPR full-waveform inversion techniques have also been developed (e.g., Ernst et al., 2007a, 2007b; Gloaguen et al., 2007; Kuroda et al., 2007).

Crosscorrelation and deconvolution methods for obtaining GPR responses

The theory of extracting the Green's function from correlations of recorded field fluctuations has become known as seismic interferometry (Schuster, 2009). Retrieving the electric-field impulse response (Green's function) between two points from correlations of thermal-noise measurements was established by Rytov and colleagues in the 1950s. They worked out the macroscopic implications of the fluctuation-dissipation theorem (Callen and Welton, 1951) and described the EM case in their book (Rytov et al., 1989). The result is that thermal noise in conductive material leads to spatial, temporal, and directional uncorrelated-noise, electric-current sources whose crosscorrelation in the frequency domain is given by the real part of the electric dissipation. This leads to the result that the crosscorrelation of thermal noise recorded at two receiving locations is proportional to the electric-field Green's function between those locations. The thermal energy is the proportionality factor. Extracting the general EM Green's function using active or passive sources, with several examples for practical implementations, is formulated by Slob and Wapenaar (2007, 2008). An example of this application for surface GPR can be found in Hanafy and Schuster (2007) and for borehole GPR in Liu and He (2007). Interferometry by crosscorrelation can be performed trace by trace, and there are no restrictions on the subsurface heterogeneity; but for all practical purposes, the conductivity should be small. A comprehensive tutorial on seismic interferometry can be found in Wapenaar et al. (2010a, 2010b).

When sources are available at one side of the receivers, which in turn are located at a certain depth level, we can use the notion of the impulse reflection response as the deconvolution of a one-way wavefield by the one-way wavefield propagating in the opposite direction. If we take up/down as the direction of separation, the sources can be assumed to be above the receivers at a certain depth level. The recorded wavefield needed to determine the energy state of the system can be decomposed into an upgoing and a downgoing wavefield at the receiver level. GPR applications are analyzed in Slob (2009), who finds that decreasing velocity structure with increasing depth leads to limited applicability of large antenna offsets. This is because the spectral width of the data is determined by the highest velocity in the medium between the sources and the receiver level. The desired spectral width of the impulse-reflection response can be larger than is available in the recorded data, and this cannot be reconstructed. The advantage of the deconvolution method is that it remains valid for strongly dissipative media, which is where the correlation method ceases to work. The disadvantage is that multicomponent data must be available at the receiver level.
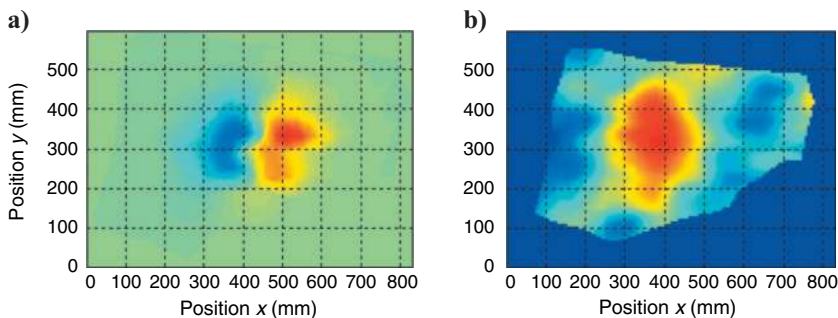

Figure 11. Visualization images of a buried PMN-2 by ALIS (02 July 2009 by PG-2 data 28, Cambodia): (a) metal detector; (b) GPR depth slice of the 3D migration image.
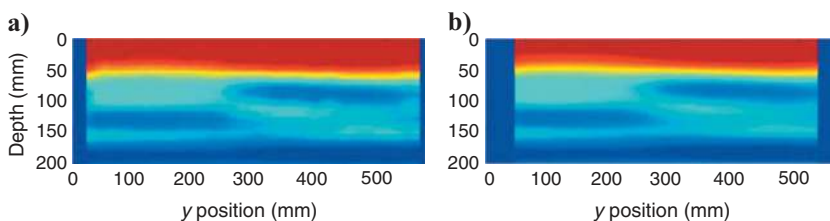

Figure 12. Radargram: (a) raw signal, (b) processed signal.

CONCLUSIONS

We have given an overview of GPR principles and uses. For many applications, the detection problem requires only recording and interpreting data. In applications that require structural subsurface information and characterization of subsurface objects, imaging and/or inversion of the recorded data is necessary. The linear model for

imaging and inversion uses all horizontal polarizations, but the model can be used on single-polarization data. Full nonlinear inversion has been developed for monostatic GPR data using a 1D earth model. For more general models, full-waveform inversion is being developed.

In borehole radar, new developments include directional borehole radar, which uses optical electric-field sensors to produce high-quality data because the passive sensors minimize the total metal content in the receiver array, resulting in good phase characteristics. When radar polarimetry is applied to subsurface fracture characterization, polarimetric borehole radar largely overcomes the low-resolution characteristics of ordinary borehole radar. We believe these new approaches will promote the possibilities of borehole radar.

The use of handheld GPR applied to humanitarian demining has been one of the successful developments of modern radar technology. A small target buried in heterogeneous soil is difficult to detect by GPR, but it can be achieved by applying 3D migration dedicated to the developed hardware.

The 3D modeling of GPR data has become a routine operation. Attention has shifted from imaging and linear inversion and tomography to full-waveform nonlinear inversion and tomography. New techniques have been developed to obtain GPR responses from crosscorrelating measured GPR data or by first performing a directional decomposition of measured GPR data and then deconvolution to obtain the earth impulse reflection response.

REFERENCES

Adcock, F., 1959, Radio direction finding in three dimensions: Proceedings of the Institute of Radio Engineers, 20, 7–11.
Allred, B. J., J. J. Daniels, and M. R. Ehsani, eds., 2008, Handbook of agricultural geophysics: CRC Press.
Annan, A. P., 1973, Radio interferometry depth sounding: Part I — Theoretical discussion: Geophysics, **38**, 557–580.
———, 2002, GPR — History, trends and future developments: Subsurface Sensing Technologies and Applications, **3**, no. 4, 253–270.
———, 2005, Ground penetrating radar, *in* D. K. Butler, ed., Near-surface geophysics: SEG, 357–438.
Arcone, S. A., 1995, Numerical studies of the radiation patterns of resistively loaded dipoles: Journal of Applied Geophysics, **33**, 39–52.
Arcone, S. A., P. R. Peapples, and L. Liu, 2003, Propagation of a ground-penetrating radar (GPR) pulse in a thin-surface waveguide: Geophysics, **68**, 1922–1933.
Bailey, J. T., S. Evans, and G. de Q. Robin, 1964, Radio echo sounding of polar ice sheets: Nature, **204**, 420–421.
Balanis, C. A., 1988, Advanced engineering electromagnetics: Wiley Interscience.
Barringer, A. R., 1965, Research directed to the determination of subsurface terrain properties and ice thickness by pulsed VHF propagation methods: Air Force Cambridge Research Laboratories contribution AF19(628)2998.
Baum, C., ed., 1998, The detection and identification of visually obscured objects: CRC Press.
Benson, R. C., 1979, Applications of ground-penetrating radar to geotechnical, hydrologic and environmental assessments: Journal of Applied Geophysics, **33**, 177–193.
Beres, M., and F. P. Haeni, 1991, Application of ground-penetrating radar methods in hydrogeologic studies: Ground Water, **29**, no. 3, 375–386.
Bevan, B. W., 1991, The search for graves: Geophysics, **56**, 1310–1319.
Bloemenkamp, R. F., and E. C. Slob, 2003a, Imaging of high-frequency full-vectorial GPR data using measured footprints: 23rd IEEE Geoscience and Remote Sensing Symposium (IGARS), 1362–1364.
———, 2003b, The effect of the elevation of GPR antennas on data quality: Proceedings of the 2nd International Workshop on Advanced Ground Penetrating Radar, 201–206.
Boltzmann, L., 1876, Zur Theorie der elastischen Nachwirkung: Annalen der Physik und Chemie, Ergaenzungsband, 7, 624–654.
Bradford, J. H., W. P. Clement, and W. Barrash, 2009, Estimating porosity with ground-penetrating radar reflection tomography: A controlled 3-D experiment at the Boise hydrogeophysical research site: Water Resources Research, **45**, W00D26.
Bristow, C., and H. Jol, eds., 2003, Ground penetrating radar in sediments: Geological Society of London.
Callen, H. B., and T. A. Welton, 1951, Irreversibility and generalized noise: Physical Review, **83**, no. 1, 34–40.
Cassidy, N. J., 2007, A review of practical numerical modelling methods for the advanced interpretation of ground-penetrating radar in near-surface environments: Near Surface Geophysics, **5**, 5–21.
Cassidy, N. J., and T. M. Millington, 2009, The application of finite-difference time-domain modeling for the assessment of GPR in magnetically lossy materials: Journal of Applied Geophysics, **67**, no. 4, 296–308.
Chanzy, A., A. Tarussov, A. Judge, and F. Bonn, 1996, Soil water content determination using digital ground penetrating radar: Soil Science Society of America Journal, **60**, 1318–1326.
Choy, T. C., 1999, Effective medium theory: Principles and applications: Clarendon Press.
Cloude, S. R., and E. Pottier, 1997, An entropy based classification scheme for land applications of polarimetric SAR: IEEE Transactions on Geoscience and Remote Sensing, **35**, no. 1, 68–78.
Collins, M. E., and J. A. Doolittle, 1987, Using ground-penetrating radar to study soil microvariability: Soil Science Society of America Journal, **51**, 491–493.
Conyers, L., and D. Goodman, eds., 1997, Ground-penetrating radar: An introduction for archaeologists: AltaMira Press.
Cook, J. C., 1977, Borehole exploration in a coal seam: Geophysics, **42**, 1254–1257.
Crocco, L., F. Soldovieri, T. Millington, and N. J. Cassidy, 2010, Bistatic tomographic GPR imaging for incipient pipeline leakage evaluation: Progress in Electromagnetics Research (PIER), **101**, 307–321.
Curlander, J. C., and R. N. McDonough, 1991, Synthetic aperture radar, systems and signal processing: Wiley Interscience.
Daniels, D. J., ed., 2004, Ground penetrating radar, 2nd ed.: Institution of Engineering and Technology.
Daniels, D. J., P. Curtis, R. Amin, and N. Hunt, 2005, MINEHOUND™ production development: Proceedings of the 10th Conference on Detection and Remediation Technologies for Mines and Minelike Targets, SPIE, 5794, 488–494.
Davis, J. L., and A. P. Annan, 1989, Ground-penetrating radar for high-resolution mapping of soil and rock stratigraphy: Geophysical Prospecting, **37**, 531–551.
Deparis, J., and S. Garambois, 2009, On the use of dispersive AVPO GPR curves for thin-bed properties estimation: Theory and application to fracture characterization: Geophysics, **74**, no. 1, J1–J12.
Diamanti, N., and A. Giannopoulos, 2009, Implementation of ADI-FDTD subgrids in ground penetrating radar FDTD models: Journal of Applied Geophysics, **67**, no. 4, 309–317.
Doerksen, K., 2002, Improved optical positioning for GPR based structure mapping: 9th Conference on Ground Penetrating Radar, SPIE, 4758, 503–507.
Doheny, R. C., S. Burke, R. Cresci, P. Ngan, and R. Walls, 2005, Handheld standoff mine detection system (HSTAMIDS) field evaluation in Thailand: Proceedings of the 10th Conference on Detection and Remediation Technologies for Mines and Minelike Targets: SPIE, 5794, 889–900.
Eisenburger, D., and V. Gundelach, 1999, GPR measurements for determining structures within salt deposits: Proceedings of the Canadian Institute of Mining Conference on Geophysical Applications in Potash Mines.
———, 2000, Borehole radar measurements in complex geological structures: Proceedings of the 8th International Conference on Ground Penetrating Radar, SPIE, 121–125.
Eisenburger, D., F. Sender, and R. Thierbach, 1993, Borehole radar — An efficient geophysical tool to aid in the planning of salt caverns and mines: 7th Symposium on Salt, Proceedings, 279–284.
Engheta, N., C. H. Papas, and C. Elachi, 1982, Radiation patterns of interfacial dipole antennas: Radio Science, **17**, 1557–1566.
Ernst, J. R., A. G. Green, H. Maurer, and K. Holliger, 2007a, Application of a new 2D time-domain full-waveform inversion scheme to crosshole radar data: Geophysics, **72**, no. 5, J53–J64.
Ernst, J. R., K. Holliger, H. Maurer, and A. G. Green, 2006, Realistic FDTD modeling of borehole georadar antenna radiation: Methodology and application: Near Surface Geophysics, **4**, 19–30.
Ernst, J. R., H. Maurer, A. G. Green, and K. Holliger, 2007b, Full-waveform inversion of crosshole radar data based on 2-D finite-difference time-domain solutions of Maxwell's equations: IEEE Transactions on Geoscience and Remote Sensing, **45**, no. 9, 2807–2828.
Federal Communications Commission, 1996, Understanding the FCC regulations for low power, non-licensed transmitters: OET Bulletin 63.
Fisher, E., G. A. McMechan, and A. P. Annan, 1992a, Acquisition and processing of wide-aperture ground-penetrating radar data: Geophysics, **57**, 495–504.
Fisher, E., G. A. McMechan, A. P. Annan, and S. W. Cosway, 1992b, Examples of reverse-time migration of single channel, ground-penetrating radar profiles: Geophysics, **57**, 577–586.
Flachenecker, G., 1978, Small transistorized receiving antennas for radar-

measurement in salt deposit: International Symposium on Antennas and Propagation, 287–290.

Gazdag, J., 1978, Wave equation migration with the phase shift method: Geophysics, **43**, 1342–1351.

Giannopoulos, A., 2005, Modelling ground penetrating radar by GprMax: Construction & Building Materials, **19**, 755–762.

———, 2008, An improved new implementation of complex frequency shifted PML for the FDTD method: IEEE Transactions on Antennas and Propagation, **56**, 2995–3000.

Gloaguen, E., B. Giroux, D. Marcotte, and R. Dimitrakopoulos, 2007, Pseudo-full-waveform inversion of borehole GPR data using stochastic tomography: Geophysics, **72**, no. 5, J43–J51.

Goodman, D., 1994, Ground-penetrating radar simulation in engineering and archaeology: Geophysics, **59**, 224–232.

Grasmueck, M., 1996, 3-D ground penetrating radar applied to fracture mapping in gneiss: Geophysics, **61**, 1050–1064.

Grasmueck, M., and D. A. Viggiano, 2007, Integration of ground-penetrating radar and laser position sensors for real-time 3-D data fusion: IEEE Transactions on Geoscience and Remote Sensing, **45**, no. 1, 130–137.

Grasmueck, M., R. Weger, and H. Horstmeyer, 2005, Full-resolution 3D GPR imaging: Geophysics, **70**, no. 1, K12–K19.

Greenfield, R. J., 1988, Modeling of electromagnetic propagation between boreholes: Proceedings of the 3rd Technical Symposium on Tunnel Detection, 156–172.

Greenhouse, J. P., M. L. Brewster, G. W. Schneider, D. J. Redman, A. P. Annan, G. R. Olhoeft, J. E. Lucius, K. A. Sander, and A. Mazzella, 1993, Geophysics and solvents: The Borden experiment: The Leading Edge, **12**, 261–267.

Hanafy, S. M., and G. T. Schuster, 2007, Target-oriented interferometric tomography for GPR data: Geophysics, **72**, no. 3, J1–J6.

Hansen, T. B., and P. M. Johansen, 2000, Inversion scheme for ground penetrating radar that takes into account the planar air-soil interface: IEEE Transactions on Geoscience and Remote Sensing, **38**, no. 1, 496–506.

His-Tien, C., 1989, Borehole directional radar system for geological mapping: Journal of Atmospheric and Terrestrial Physics, **51**, 819–828.

Holliger, K., and T. Bergmann, 1998, Accurate and efficient FDTD modeling of ground penetrating radar antenna radiation: Geophysical Research Letters, **25**, no. 20, 3883–3886.

———, 2002, Numerical modeling of borehole georadar data: Geophysics, **67**, 1249–1257.

Holloway, A. L., N. M. Soonawala, and L. S. Collett, 1986, Three-dimensional fracture mapping in granite excavations using ground-penetrating radar: Canadian Institute of Mining, Metallurgy and Petroleum Bulletin, **79**, 54–59.

Huisman, J. A., S. S. Hubbard, J. D. Redman, and A. P. Annan, 2003, Measuring soil water content with ground penetrating radar: A review: Vadose Zone Journal, **2**, 476–491.

Irving, J., and R. Knight, 2005, Effects of antennas on velocity estimates obtained from crosshole GPR data: Geophysics, **70**, no. 5, K39–K42.

———, 2006, Numerical simulation of antenna transmission and reception for crosshole ground-penetrating radar: Geophysics, **71**, no. 2, K37–K45.

Irving, J., R. Knight, and K. Holliger, 2009, Estimation of the lateral correlation structure of subsurface water content from surface-based ground-penetrating radar reflection images: Water Resources Research, **45**, no. 12, W12404.

Jol, H. M., ed., 2009, Ground penetrating radar theory and applications: Elsevier Science.

Jones, E. M., and K. Glover, 2007, Apollo lunar roving vehicle documentation: Apollo Lunar Surface Journal, posted 10 September 2007, http://history.nasa.gov/alsj/alsj-LRVdocs.html, accessed 22 July 2010.

King, R. W. P., and G. L. Smith, 1981, Antennas in matter: MIT Press.

Kuroda, S., M. Takeuchi, and H. J. Kim, 2007, Full-waveform inversion algorithm for interpreting crosshole radar data: A theoretical approach: Geosciences Journal, **11**, no. 3, 211–217.

Lambot, S., F. André, K. Z. Jadoon, E. C. Slob, and H. Vereecken, 2010, Full-waveform modeling of ground-coupled GPR antennas for wave propagation in multilayered media: The problem solved? Proceedings of the 13th International Conference on Ground Penetrating Radar, 898–902.

Lambot, S., J. Rhebergen, I. van den Bosch, E. C. Slob, and M. Vanclooster, 2004a, Measuring the soil water content profile of a sandy soil with an off-ground monostatic ground penetrating radar: Vadose Zone Journal, **3**, 1063–1071.

Lambot, S., E. Slob, D. Chavarro, M. Luczynski, and H. Vereecken, 2008, Measuring soil surface water content in irrigated areas of southern Tunis using full-waveform inversion of proximal GPR data: Near Surface Geophysics, **6**, 403–410.

Lambot, S., E. C. Slob, J. Rhebergen, O. Lopera, K. Z. Jadoon, and H. Vereecken, 2009, Remote estimation of the hydraulic properties of a sand using full-waveform integrated hydrogeophysical inversion of time-lapse, off-ground GPR data: Vadose Zone Journal, **8**, 743–754.

Lambot, S., E. C. Slob, I. van den Bosch, B. Stockbroeck, and M. Vanclooster, 2004b, Modeling of ground-penetrating radar for accurate char-

acterization of subsurface electric properties: IEEE Transactions on Geoscience and Remote Sensing, **42**, 2555–2568.

Lampe, B., K. Holliger, and A. G. Green, 2003, A finite-difference time-domain simulation tool for ground-penetrating radar antennas: Geophysics, **68**, 971–987.

Leatherman, S. P., 1987, Coastal geomorphological applications of ground-penetrating radar: Journal of Coastal Research, **3**, 397–399.

Lehmann, F., D. E. Boerner, K. Holliger, and A. G. Green, 2000, Multicomponent georadar data: Some important implications for data acquisition and processing: Geophysics, **65**, 1542–1552.

Lehmann, F., and A. G. Green, 1999, Semi-automated georadar data acquisition in three dimensions: Geophysics, **64**, 719–731.

———, 2000, Topographic migration of georadar data: Implications for acquisition and processing: Geophysics, **65**, 836–848.

Liu, C., and L. C. Shen, 1991, Numerical simulation of subsurface radar for detecting buried pipes: IEEE Transactions on Geoscience and Remote Sensing, **29**, 795–798.

Liu, L. B., and K. He, 2007, Wave interferometry applied to borehole radar: Virtual multioffset reflection profiling: IEEE Transactions on Geoscience and Remote Sensing, **45**, 2554–2559.

Liu, S., and M. Sato, 2005, Transient radiation from an unloaded, finite dipole antenna in a borehole: Experimental and numerical results: Geophysics, **70**, no. 6, K43–K51.

Lopera, O., E. C. Slob, N. Milisavljević, and S. Lambot, 2007, Filtering soil surface and antenna effects from GPR data to enhance landmine detection: IEEE Transactions on Geoscience and Remote Sensing, **45**, 707–717.

Lytle, R. J., and E. F. Laine, 1978, Design of a miniature directional antenna for geophysical probing from boreholes: IEEE Transactions on Geoscience and Remote Sensing, **16**, 304–307.

Lytle, R. J., E. F. Laine, D. L. Lager, and D. T. Davis, 1979, Cross-borehole electromagnetic probing to locate high-contrast anomalies: Geophysics, **44**, 1667–1676.

Maser, K. R., 1986, Detection of progressive deterioration in bridge decks using ground penetrating radar: Experimental assessment of the performance of bridges: Proceedings of the American Society of Civil Engineers/Engineering Mechanics Division Specialty Conference, 42–57.

Maser, K., and T. Scullion, 1992, Automated pavement subsurface profiling using radar: Case studies of four experimental field sites: Transportation Research Record, **1344**, 148–154.

Milton, G. W., 2002, The theory of composites: Cambridge University Press.

Minet, J., S. Lambot, E. Slob, and M. Vanclooster, 2010, Soil surface water content estimation by full-waveform GPR signal inversion in the presence of thin layers: IEEE Transactions on Geoscience and Remote Sensing, **48**, 1138–1150.

Mundry, E., F. Sender, R. Thierbach, and H. Weichart, 1983, Borehole radar probing in salt deposits: Proceedings of the 6th International Symposium on Salt, The Salt Institute, 585–599.

Nickel, H., F. Sender, R. Thierbach, and H. Weichart, 1983, Exploring the interior of salt domes from boreholes: Geophysical Prospecting, **31**, no. 1, 131–148.

Niva, B., O. Olsson, and P. Blueming, 1988, Radar cross hole tomography with application to migration of saline tracer through fracture zones, Grimsel Test Site: Swiss National Cooperative for the Storage of Nuclear Waste (NAGRA) Technical Report 88-31.

Noon, D. A., G. F. Stickley, and D. Longstaff, 1998, A frequency-independent characterisation of GPR penetration and resolution performance: Journal of Applied Geophysics, **40**, no. 1–3, 127–137.

Oden, C. P., G. R. Olhoeft, D. L. Wright, and M. H. Powers, 2008, Measuring the electrical properties of soil using a calibrated ground-coupled GPR system: Vadose Zone Journal, **7**, no. 1, 171–183.

Olhoeft, G. R., 1980, Thawing of permafrost along the Trans-Alaska pipeline: Proceedings of the Symposium on Permafrost Geophysics: Ottawa, Canada, Nuclear Regulatory Commission Technical Memo, 128, 103–109.

———, 1987, Electrical properties from 10^{-3} to 10^{+9} Hz — Physics and chemistry: Proceedings of the 2nd International Symposium on the Physics and Chemistry of Porous Media, American Institute of Physics, 281–298.

———, 1988, Interpretation of hole-to-hole radar measurements: Proceedings of the 3rd Technical Symposium on Tunnel Detection, 616–629.

———, 1991a, Quantitative statistical description of subsurface heterogeneities with ground penetrating radar at Bemidji, Minnesota: USGS Water-Resources Investigations Report 91–4034, 650–653.

———, 1991b, Spatial variability: Proceedings of the National Science Foundation/Electric Power Research Institute Workshop on Dynamic Soil Properties and Site Characterization, Report NP-7337, 5-1–5-20.

———, 1993, Velocity, attenuation, dispersion and diffraction hole-to-hole radar processing: Proceedings of the 4th Tunnel Detection Symposium on Subsurface Exploration Technology, 309–322.

———, 1994, Modeling out-of-plane scattering effects: Proceedings of the 5th International Conference on Ground Penetrating Radar, 133–144.

———, 1999, Applications and frustrations in using ground penetrating radar:

Proceedings of the Ultra Wideband Conference, on CD-ROM.

———, 2000, Maximizing the information return from ground penetrating radar: Journal of Applied Geophysics, **43**, no. 2–4, 175–187.

Olhoeft, G. R., and D. E. Capron, 1994, Petrophysical causes of electromagnetic dispersion: Proceedings of the 5th International Conference on Ground Penetrating Radar, 145–152.

Olhoeft, G. R., M. H. Powers, and D. E. Capron, 1994, Buried object detection with ground penetrating radar: Proceedings of Unexploded Ordnance (UXO) Detection and Range Remediation Conference, 207–233.

Olhoeft, G. R., S. Smith III, J. P. Hyslip, and E. T. Selig, 2004, GPR in railroad investigations: Proceedings of the 10th International Conference on Ground Penetrating Radar, 635–638.

Olsson, O., L. Falk, O. Forslund, L. Lundmark, and E. Sandberg, 1992, Borehole radar applied to the characterization of hydraulically conductive fracture-zones in crystalline rock: Geophysical Prospecting, **40**, no. 2, 109–142.

Olsson, O., E. Sandberg, O. Forslund, L. Lundmark, and L. Falk, 1985, The mapping of fracture zones by borehole radar: Geoexploration, **23**, no. 3, 427–428.

Orlando, L., and E. C. Slob, 2009, Using multicomponent GPR to monitor cracks in a historical building: Journal of Applied Geophysics, **67**, 327–334.

Owen, T. E., and S. E. Suhler, 1982, Borehole directional radar detection of subsurface cavities: Geophysics, **47**, 416–416.

Owsley, D. W., 1995, Techniques for locating burials, with emphasis on the probe: Journal of Forensic Sciences, **40**, 735–740.

Paulino, N., J. Goes, and A. S. Garcao, 2008, Low power UWB CMOS sensors: Springer.

Redheffer, R., 1961, Difference equations and functional equations in transmission line theory: McGraw-Hill Book Co.

Redman, J., J. Davis, L. Galagedara, and G. Parkin, 2002, Field studies of GPR air launched surface reflectivity measurements of soil water content: Proceedings of the 9th International Conference on Ground Penetrating Radar, SPIE, 4758, 156–161.

Robin, G. de Q., S. Evans, and J. T. Bailey, 1969, Interpretation of radio echo sounding in polar ice sheets: Philosophical Transactions of the Royal Society of London, Series A, **265**, 437–505.

Rodeick, C. A., 1984, Roadbed void detection by ground penetrating radar: Highway & Heavy Construction, **127**, 60–61.

Rytov, S. M., Y. A. Kravtsov, and V. I. Tatarskii, 1989, Principles of statistical radiophysics: Springer-Verlag Berlin.

Sander, K. A., G. R. Olhoeft, J. E. Lucius, 1992, Surface and borehole radar monitoring of a DNAPL spill in 3D versus frequency, look angle and time: Proceedings of the Symposium on the Application of Geophysics to Engineering and Environmental Problems (SAGEEP), 455–469.

Sandness, G. A., and C. S. Kimball, 1982, Ground-penetrating radar in characterizing and monitoring waste burial sites: Transactions of the American Nuclear Society, **41**, 71–72.

Sato, M., 2005, Dual sensor ALIS evaluation test in Afghanistan: IEEE Geoscience and Remote Sensing Society Newsletter, **136**, 22–27.

———, 2009, ALIS evaluation tests in Croatia: Proceedings of the 10th Conference on Detection and Remediation Technologies for Mines and Minelike Targets, SPIE, 7303, 730731B-1–73031B-12.

Sato, M., J. Fujiwara, and K. Takahashi, 2007, The development of the handheld dual-sensor ALIS: Proceedings of the 12th Conference on Detection and Remediation Technologies for Mines and Minelike Targets: SPIE, 6553, 65531C.

Sato, M., and T. Takayama, 2007, A novel directional borehole radar system using optical electric field sensors: IEEE Transactions on Geoscience and Remote Sensing, **45**, 2529–2535.

Sato, M., and R. Thierbach, 1991, Analysis of a borehole radar in cross-hole mode: IEEE Transactions on Geoscience and Remote Sensing, **29**, 899–904.

Schaber, G. G., J. F. McCauley, C. S. Breed, and G. R. Olhoeft, 1986, Shuttle imaging radar: Physical controls on signal penetration and subsurface scattering in the eastern Sahara: IEEE Transactions on Geoscience and Remote Sensing, **GE-24**, 603–623.

Schenk, C. J., D. L. Gautier, G. R. Olhoeft, and J. E. Lucius, 1993, Internal structure of an eolian dune using ground penetrating radar, *in* K. Pye and N. Lancaster, eds., Aeolian sediments: Ancient and modern: International Association of Sedimentologists Special Publication 16, 61–69.

Schuster, G., 2009, Seismic interferometry: Cambridge University Press.

Scott, L. D., and H. T. Chang, 1984, Field pattern for antennas situated in a borehole: IEEE International Symposium on Antennas and Propagation, 113–116.

Serbin, G., and D. Or, 2003, Near surface water content measurements using horn antenna radar: Methodology and overview: Vadose Zone Journal, **2**, 500–510.

———, 2004, Ground-penetrating radar measurement of soil water content dynamics using a suspended horn antenna: IEEE Transactions on Geoscience and Remote Sensing, **42**, 1695–1705.

Sihvola, A., 1999, Electromagnetic mixing formulas and applications: Institution of Engineering and Technology.

Simmons, G., D. W. Strangway, L. Bannister, R. Baker, D. Cubley, G. La Torraca, and R. Watts, 1972, The surface electrical properties experiment, *in* Z. Kopal and D. W. Strangway, eds., Lunar geophysics: D. Reidel Publ. Co., 258–271.

Slob, E., 2009, Interferometry by deconvolution of multicomponent multi-offset GPR data: IEEE Transactions on Geoscience and Remote Sensing, **47**, 828–838.

Slob, E. C., R. Bloemenkamp, and A. G. Yarovoy, 2003a, Efficient computation of the wavefield in a two-media configuration emitted by a GPR system from incident field measurements in the air: Proceedings of the 2nd International Workshop on Advanced Ground Penetrating Radar, 60–65.

Slob, E. C., J. Groenenboom, and J. T. Fokkema, 2003b, Automated acquisition and processing of 3D GPR data for object detection and characterization: Subsurface Sensing Technologies and Applications, **4**, no. 1, 5–18.

Slob, E., and K. Wapenaar, 2007, Electromagnetic Green's functions retrieval by cross-correlation and cross-convolution in media with losses: Geophysical Research Letters, **34**, L05307.

———, 2008, Practical representations of electromagnetic interferometry for GPR applications: Near Surface Geophysics, **6**, 391–402.

Smith, G. S., 1984, Directive properties of antennas for transmission into a material half-space: IEEE Transactions on Antennas and Propagation, **32**, no. 3, 232–246.

———, 1997, An introduction to classical electromagnetic radiation: Cambridge University Press.

Stern, W., 1929, Versuch einer elektrodynamischen Dickenmessung von Gletschereis: Beiträge zur Geophysik, **23**, 292–333.

Stolt, R. H., 1978, Migration by Fourier transform: Geophysics, **43**, 23–48.

Streich, R., and J. van der Kruk, 2007, Accurate imaging of multicomponent GPR data based on exact radiation patterns: IEEE Transactions on Geoscience and Remote Sensing, **45**, no. 1, 93–103.

Streich, R., J. van der Kruk, and A. G. Green, 2007, Vector-migration of standard copolarized 3D GPR data: Geophysics, **72**, no. 5, J65–J75.

Strobbia, C., and G. Cassiani, 2007, Multilayer ground-penetrating radar guided waves in shallow soil layers for estimating soil water content: Geophysics, **72**, no. 4, J17–J29.

Takahashi, K., and M. Sato, 2006, Parametric inversion technique for location of cylindrical structures by cross-hole measurements: IEEE Transactions on Geoscience and Remote Sensing, **44**, no. 11, 3348–3355.

Takayama, T., and M. Sato, 2007, A novel direction-finding algorithm for directional borehole radar: IEEE Transactions on Geoscience and Remote Sensing, **45**, no. 8, 2520–2528.

Taylor, J. D., ed., 1995, An introduction to ultra-wideband systems: CRC Press.

Teixeira, F. L., and W. C. Chew, 2000, Finite-difference computation of transient electromagnetic waves for cylindrical geometries in complex media: IEEE Transactions on Geoscience and Remote Sensing, **38**, 1530–1543.

Teixeira, F. L., W. C. Chew, M. Straka, M. L. Oristaglio, and T. Wang, 1998, Finite-difference time-domain simulation of ground-penetrating radar in dispersive, inhomogeneous, and conductive soils: IEEE Transactions on Geoscience and Remote Sensing, **36**, 1928–1937.

Thierbach, R., 1974, Electromagnetic reflections in salt deposits: Journal of Geophysics, **40**, 633–637.

Tsang, L., J. A. Kong, and R. T. Shin, 1985, Theory of microwave remote sensing: Wiley Interscience.

Ulaby, F. T., R. K. Moore, and A. K. Fung, 1982, Microwave remote sensing, vol. 2: Addison-Wesley Publ. Co., 746–1033.

van Dam, R. L., and W. Schlager, 2000, Identifying causes of ground-penetrating radar reflections using time-domain reflectometry and sedimentological analysis: Sedimentology, **47**, 435–449.

van Dam, R. L., W. Schlager, M. J. Dekkers, and J. A. Huisman, 2002, Iron oxides as a cause of GPR reflections: Geophysics, **67**, 536–545.

van der Kruk, J., S. A. Arcone, and L. Liu, 2007, Fundamental and higher mode inversion of dispersed GPR waves propagating in an ice layer: IEEE Transactions on Geoscience and Remote Sensing, **45**, 2483–2491.

van der Kruk, J., C. M. Steelman, A. L. Endres, and H. Vereecken, 2009, Dispersion inversion of electromagnetic pulse propagation within freezing-thawing soil waveguides: Geophysical Research Letters, **36**, L18503.

van der Kruk, J., C. J. Wapenaar, J. T. Fokkema, and P. M. van den Berg, 2003, Three-dimensional imaging of multi-component ground-penetrating radar data: Geophysics, **68**, 1241–1254.

van Dongen, K. W. A., P. M. van den Berg, and I. Nicolaescu, 2004, Subsurface imaging using measured near-field antenna footprints: Near Surface Geophysics, **2**, 33–39.

van Dongen, K. W. A., R. van Waard, S. van der Baan, P. M. van den Berg, and J. T. Fokkema, 2002, A directional borehole radar system: Subsurface Sensing Technologies and Applications, **3**, no. 4, 327–346.

van Gestel, J. P., and P. L. Stoffa, 2001, Application of Alford rotation to ground-penetrating radar data: Geophysics, **66**, 1781–1792.

van Zyl, J. J., and F. T. Ulaby, 1990, Scattering matrix representation for simple targets, *in* F. T. Ulaby, and C. Elachi, eds., Radar polarimetry for geo-

science applications: Artech House, 17–52.

Vaughan, C. J., 1986, Ground penetrating radar surveys used in archaeological investigations: Geophysics, **51**, 595–604.

von Hippel, A. R., 1954, Dielectrics and waves: John Wiley & Sons, Inc.

Wang, T., and M. L. Oristaglio, 2000, GPR imaging using the generalized Radon transform: Geophysics, **65**, 1553–1559.

Wapenaar, K., D. Draganov, R. Snieder, and A. Curtis, 2010a, Tutorial on seismic interferometry, Part I: Basic principles: Geophysics, **75**, this issue.

Wapenaar, K., E. Slob, R. Snieder, and A. Curtis, 2010b, Tutorial on seismic interferometry, Part II: Underlying theory and new advances: Geophysics, **75**, this issue.

Warren, C., and A. Giannopoulos, 2009, Optimising models of commercial GPR antennas: Proceedings of the 5th International Workshop on Advanced Ground Penetrating Radar, 18–22.

Witten, A. J., J. E. Molyneux, and J. E. Nyquist, 1994, Ground-penetrating radar tomography — Algorithms and case studies: IEEE Transactions on Geoscience and Remote Sensing, **32**, 461–467.

Yi, M., J. Kim, S. Cho, and M. Sato, 2005, Integrated application of borehole radar reflection and resistivity tomography to delineate fractures at a granite quarry: Subsurface Sensing Technologies and Applications, **6**, no. 1, 89–100.

Yilmaz, O., 2001, Seismic data analysis, 2nd ed.: SEG.

Zhao, J., and M. Sato, 2006, Radar polarimetry analysis applied to single-hole fully polarimetric borehole radar: IEEE Transactions on Geoscience and Remote Sensing, **44**, no. 12, 3547–3554.

Zhou, H., and M. Sato, 2004, Subsurface cavity imaging by crosshole borehole radar measurements: IEEE Transactions on Geoscience and Remote Sensing, **42**, no. 2, 335–341.